



**HAL**  
open science

# Efficient simulation of single and poly-crystal plasticity based on the pencil glide mechanism

Lu Tuan Le, Kais Ammar, Samuel Forest

► **To cite this version:**

Lu Tuan Le, Kais Ammar, Samuel Forest. Efficient simulation of single and poly-crystal plasticity based on the pencil glide mechanism. *Comptes Rendus. Mécanique*, 2020, 348 (10-11), pp.847-876. 10.5802/crmeca.44> . hal-03381730

**HAL Id: hal-03381730**

**<https://hal.science/hal-03381730>**

Submitted on 17 Oct 2021

**HAL** is a multi-disciplinary open access archive for the deposit and dissemination of scientific research documents, whether they are published or not. The documents may come from teaching and research institutions in France or abroad, or from public or private research centers.

L'archive ouverte pluridisciplinaire **HAL**, est destinée au dépôt et à la diffusion de documents scientifiques de niveau recherche, publiés ou non, émanant des établissements d'enseignement et de recherche français ou étrangers, des laboratoires publics ou privés.



INSTITUT DE FRANCE  
Académie des sciences

# *Comptes Rendus*

---

## *Mécanique*

Lu Tuan Le, Kais Ammar and Samuel Forest

**Efficient simulation of single and poly-crystal plasticity based on the pencil glide mechanism**

Volume 348, issue 10-11 (2020), p. 847-876.


<https://doi.org/10.5802/crmeca.44>

**Part of the Thematic Issue:** Contributions in mechanics of materials

**Guest editors:** Julie Diani, Olivier Castelnau and Francisco Chinesta

© Académie des sciences, Paris and the authors, 2020.

*Some rights reserved.*

 This article is licensed under the  
CREATIVE COMMONS ATTRIBUTION 4.0 INTERNATIONAL LICENSE.  
<http://creativecommons.org/licenses/by/4.0/>



*Les Comptes Rendus. Mécanique sont membres du  
Centre Mersenne pour l'édition scientifique ouverte*  
[www.centre-mersenne.org](http://www.centre-mersenne.org)



---

Contributions in mechanics of materials

# Efficient simulation of single and poly-crystal plasticity based on the pencil glide mechanism

Lu Tuan Le<sup>a</sup>, Kais Ammar<sup>a</sup> and Samuel Forest<sup>\*, a</sup>

<sup>a</sup> MINES ParisTech, PSL University, Centre des matériaux (CMAT), CNRS UMR 7633, BP 87 91003 Evry, France

*E-mails:* lutuan.le@gmail.com (L. T. Le), kais.ammar@mines-paristech.fr (K. Ammar), samuel.forest@mines-paristech.fr (S. Forest)

**Abstract.** The present work demonstrates that the pencil glide mechanism is a physically reliable and a computationally efficient model to simulate the nonlinear behaviour of b.c.c. single and polycrystals. For that purpose, the pencil glide extension of Schmid's criterion used by Gilormini [1] is incorporated in a single crystal model and in a homogenized polycrystal model accounting for large elastoviscoplastic deformations. The response of the pencil glide model in terms of stress-strain curves and lattice rotation is compared to the prediction based on the consideration of all  $\{110\}\langle 111\rangle + \{112\}\langle 111\rangle$  slip systems. In the case of  $\alpha$ -iron single crystals both approaches are shown to accurately reproduce recent experimental results [2, 3]. The comparison is extended to  $\alpha$ -iron polycrystals behaviour under tension, compression, rolling and simple shear loading conditions. The evolution of crystallographic textures obtained either based on pencil glide or using the 24 slip systems is analyzed and compared to classical experimental results from the literature. Limitations of the approach, especially in the case of simple shear textures, are also pointed out. The pencil glide approach can be viewed as a reduced order model enhancing computational efficiency of crystal plasticity simulations involving many slip mechanisms.

**Keywords.** Crystal plasticity, Pencil glide, Single crystal, Polycrystal, b.c.c. crystal, Homogenization, Texture.

*Manuscript received 10th June 2020, accepted 30th July 2020.*

## 1. Introduction

Many crystals with b.c.c. (body centered cubic) structure exhibit a specific plastic behaviour at low temperature characterized by the difficulty of identifying the slip planes along which dislocations are gliding, whereas the slip direction (given by the Burgers vector) is clearly defined. The reason is that screw dislocations can easily cross-slip on several planes containing each slip

---

\* Corresponding author.

direction which is a zone axis of the crystal. Slip lines are observed to be sinuous and this phenomenon was called *pencil glide* and *non-crystallographic slip* by Taylor and Elam [4]. Modifications of the well-known Schmid law for crystal plasticity were proposed to accommodate pencil glide and used to predict yield surfaces of polycrystals [5]. Gilormini [1] and Becker [6] applied such a theory to predict rolling textures based on a homogenization polycrystal approach. According to the pencil glide model used in [1], the Schmid law is applied to slip systems with fixed crystallographic slip directions and optimized slip plane to maximize the resolved shear stress at each strain increment. Rolling textures were predicted in [1] using the Taylor model [7] and the relaxed constraint model [8]. It was shown that the results of the latter model were in better agreement with experimental findings [1]. However, these two homogenization techniques are known to provide bounds of the actual behaviour. From a computational perspective, an advantage of the pencil glide model is to reduce the number of slip systems and associated internal variables and corresponding material parameters. This is the main incentive of the present contribution.

Hill [9], Mecking [10, 11], Kocks [12], van Houtte [13] and Arminjon [14, 15] have proposed several classes of polycrystal models allowing for non homogeneous stress and strain values between the various orientation classes of grains. These models essentially lead to deformation textures in good agreement with measured ones. Depending on specific weighting parameters present in these models, they can account for the whole span of the solution domain between the lower and upper bounds. Another class of non-homogeneous models which make use of the Eshelby theory to estimate the local stress and strain is the viscoplastic self-consistent scheme (VPSC) [16, 17]. All grains having the same orientation within a given precision are gathered in a single monocrystalline inclusion embedded in the effective medium. This reflects explicitly some nonlinear interaction of each grain with its homogenized surroundings [18]. For the quasi-rate-independent case, there also exists a self-consistent polycrystal plasticity model relying on the multiplicative decomposition of the deformation gradient, see [19].

In the present work, a fast computational homogenization polycrystal model is introduced, the so-called  $\beta$ -model which is a tunable extension of the Standard Self-Consistent (SSC) scheme to investigate the elasto-plasticity of polycrystals [20–25]. The grain/aggregate interaction is still taken into account via the use of the Eshelby tensor. The  $\beta$ -model incorporates interphase accommodation variables  $\beta^{(g)}$  to replace the local plastic strain  $\epsilon_p^{(g)}$  in usual SSC localization formula. The evolution law for the  $\beta$ -variables contains tunable transition parameters to be calibrated from full-field simulations of polycrystalline aggregates [26]. The  $\beta$ -model formulation from [23] is extended in the present work to allow for finite deformations using the concept of local objective frames [21]. The evolution texture in b.c.c. metals is simulated using the  $\beta$ -model. In the simulations presented in this work, we consider either the restricted glide ( $\{110\}\langle 111 \rangle + \{112\}\langle 111 \rangle$ ) or the pencil glide  $\langle 111 \rangle$  as the plastic slip modes. The responses of these mechanisms will be compared for single and poly-crystals for various loading conditions in order to assess the ability of the pencil glide model to mimic the response of the full slip model.

The article is organized as follows. First, the finite deformation framework and the pencil glide model are depicted. The polycrystal homogenization  $\beta$ -model is then presented in the case of large deformations. The third section is dedicated to the comparison of the responses of the pencil glide model and the consideration of all ( $\{110\}\langle 111 \rangle + \{112\}\langle 111 \rangle$ ) slip systems in the case of single crystals in tension and compression. In the case of polycrystals treated in Section 4, it is first necessary to calibrate the free parameters of the  $\beta$ -model from a full field simulation of polycrystalline aggregates. Polycrystal simulations are then performed in the case of tension, compression, torsion and simple shear loading conditions, considering either pencil glide or the 24 slip systems. Results are compared in terms of overall stress-strain curves, lattice rotation and evolution of texture components. Computation time of simulations for 1000 grains is also an important information provided in this work.

In the following paper, an orientation is given by the three Euler angles  $\varphi_1, \Phi, \varphi_2$  where the Bunge notation is used. The distribution of orientations, the pole figures and the ODF (Orientation Distribution Functions) maps are obtained by means of the ATEX software (<http://www.atex-software.eu/>).

## 2. Model description

### 2.1. Single crystal plasticity at large deformations

The formulation of the present single crystal plasticity model makes use of local objective frames to develop constitutive models at finite strains [27]. It was proposed in [21] for single and polycrystals and used recently in [28]. It departs from Mandel's classical formulation relying on the multiplicative decomposition of the deformation gradient  $\mathbf{F}$  [29]. The velocity gradient  $\mathbf{L}$  is decomposed into its symmetric part  $\{\mathbf{L}\}$  defining the strain rate tensor, and its skew-symmetric part  $\}\mathbf{L}\{$ , called spin tensor. The time-dependent rotation  ${}^c\mathbf{Q}$  linking the corotational space frame to the current one is defined as

$${}^c\dot{\mathbf{Q}}{}^c\mathbf{Q}^T = \}\mathbf{L}\{ \quad \text{and} \quad {}^c\mathbf{Q}(\mathbf{t} = \mathbf{0}) = \mathbf{1}. \quad (1)$$

The strain rate tensor is pulled back to the corotational frame and split into elastic and viscoplastic parts:

$${}^c\mathbf{D} = {}^c\mathbf{Q}^T \{\mathbf{L}\} {}^c\mathbf{Q} = \dot{\mathbf{e}}^e + \dot{\mathbf{e}}^p. \quad (2)$$

The Cauchy stress tensor  $\boldsymbol{\sigma}$  and the corotational stress  $\mathbf{S}$  are computed from the following elastic law:

$$\mathbf{S} = \mathbb{C} : \mathbf{e}^e, \quad \text{with} \quad \mathbf{S} = \det(\mathbf{F}) {}^c\mathbf{Q}^T \boldsymbol{\sigma} {}^c\mathbf{Q} \quad (3)$$

where  $\mathbb{C}$  denotes the fourth order tensor of elastic moduli.

Plastic deformation is the result of the contribution of all gliding slip systems of the crystal:

$$\dot{\mathbf{e}}^p = \sum_{s \in S} \dot{\gamma}^s \{ {}^c\mathbf{m}^s \otimes {}^c\mathbf{n}^s \} \quad (4)$$

where  ${}^c\mathbf{m}^s$  and  ${}^c\mathbf{n}^s$  respectively are the slip direction and the normal to the slip plane for slip system  $s$  in the corotational space frame,  $\gamma^s$  being the associated slip amount.

The link between the lattice space frame and the corotational space frame is the rotation  ${}^{\#}\mathbf{Q}$  defined as

$${}^{\#}\dot{\mathbf{Q}}{}^{\#}\mathbf{Q}^T = \sum_{s \in S} \dot{\gamma}^s \{ {}^{\#}\mathbf{m}^s \otimes {}^{\#}\mathbf{n}^s \} \quad \text{and} \quad {}^{\#}\mathbf{Q}(\mathbf{t} = \mathbf{0}) = \mathbf{Q}_0 \quad (5)$$

whose initial value depends on the initial crystal orientation. Crystallographic directions are known in the lattice frame:  ${}^{\#}\mathbf{m}^s = {}^{\#}\mathbf{Q}\mathbf{m}^s$  and  ${}^{\#}\mathbf{n}^s = {}^{\#}\mathbf{Q}\mathbf{n}^s$ . The rotation is calculated by using the exponential map described in Appendix A.

### 2.2. Pencil glide

The directions along which slip can occur in b.c.c crystals are  $\langle 111 \rangle$  with associated unit vectors  $\mathbf{m}^k$ ,  $k = 1, 2, 3, 4$ . Slip under pencil glide conditions can occur on any plane with normal  $\mathbf{n}^k$  which is parallel to one given  $\mathbf{m}^k$  vector. The driving force for plastic slip along the slip system is the resolved shear stress  $\tau^k$  computed as

$$\tau^k = (\mathbf{S}\mathbf{n}^k) \cdot \mathbf{m}^k = (\mathbf{S}\mathbf{m}^k) \cdot \mathbf{n}^k. \quad (6)$$

According to the pencil glide theory [5, 30, 31], the most probable active slip plane is the one(s) maximizing the value of the resolved shear stress. This optimization procedure provides the following formula, valid for non-vanishing shear stress:

$$\mathbf{n}^k = \frac{\mathbf{m}^k \times (\mathbf{S}\mathbf{m}^k) \times \mathbf{m}^k}{\tau^k} \tag{7}$$

which implies that

$$\tau^k = \|\mathbf{m}^k \times (\mathbf{S}\mathbf{m}^k)\|. \tag{8}$$

### 2.3. Hardening mechanisms

The plastic slip rate  $\dot{\gamma}$  for a pencil glide slip system  $s$  is expressed by a rate-dependent phenomenological flow rule. The following classical form, taken for example from [32], is adopted:

$$\dot{\gamma}^s = \left\langle \frac{|\tau^s| - r^s}{K} \right\rangle^n \text{sign}(\tau^s). \tag{9}$$

The material parameters  $K$  and  $n$  characterize the viscosity, and  $r^s$  is the critical resolved shear stress including the following form of isotropic hardening, according to [33]:

$$r^s = r_0 + Q \sum_l h^{sl} (1 - \exp(-bv^l)), \quad \text{with } v^l = |\dot{\gamma}^l|. \tag{10}$$

Here,  $r_0$  denotes the initial critical resolved shear stress,  $Q$ ,  $b$  are material hardening parameters,  $h^{sl}$  is the interaction matrix which represents self-hardening and latent hardening. It must be noted that, due to the fact that slip plane is likely to change at each load increment, the slip variable integrated from (9) has no real crystallographic meaning and rather is a nonholonomic cumulative slip variable depending on the path.

### 2.4. Polycrystal homogenization: the $\beta$ -model

Gilormini [1] has used the pencil glide mechanism to predict the rolling textures in b.c.c. polycrystals with the Taylor model. The Taylor model provides qualitative agreement with some experimental results. However other polycrystal homogenization schemes are eligible for the use of the pencil glide model. In the present work, a generic homogenization model for polycrystals is applied, namely the  $\beta$ -model which can be regarded as a class of reduced order models [20, 23–25, 32, 34, 35]. The approach is based on the introduction of an interphase accommodation variable  $\boldsymbol{\beta}^{(g)}$  related to the mean plastic strain  $\mathbf{e}_p^{(g)}$  in each grain orientation number  $g$ . Still using (1) to (3), the stress tensor in the corotational frame is computed by means of the effective (homogenized) tensor of elastic moduli:

$$\mathbf{S} = \mathbb{C}_{\text{Homo}} : \mathbf{e}^e. \tag{11}$$

The self-consistent homogenization model is used to compute the effective moduli  $\mathbb{C}_{\text{Homo}}$  as the limit of the series:

$$\mathbb{C}_{\text{Homo}}(n) = \sum_g f_{(g)} \mathbb{C}^{(g)} : [\mathbb{I} - \mathbb{S}_{\text{Esh}}(n-1) : (\mathbb{I} - \mathbb{C}_{\text{Homo}}^{-1}(n-1) : \mathbb{C}^{(g)})] \tag{12}$$

with  $\mathbb{C}_{\text{Homo}}(0) = \sum_g f_{(g)} \mathbb{C}^{(g)}$ ,  $f_{(g)}$  being the volume fraction of grain orientation  $g$ . The equations to compute  $\mathbb{S}_{\text{Esh}}$  are detailed in Appendix B.

The following scale transition rule is adopted to compute the mean stress for each grain orientation  $g$ :

$$\mathbf{s}^{(g)} = \mathbb{B}^{(g)} : (\mathbf{S} + \mathbb{L}_C^* : (\boldsymbol{\beta} - \boldsymbol{\beta}^{(g)})) \tag{13}$$

where  $\mathbb{B}^{(g)}$  is the localization tensor defined as

$$\mathbb{B}^{(g)} = \mathbb{C}^{(g)} : [\mathbb{I} + \mathbb{S}_{\text{Esh}} : \mathbb{C}_{\text{Homo}}^{-1} : (\mathbb{C}^{(g)} - \mathbb{C}_{\text{Homo}})]^{-1} : \mathbb{C}_{\text{Homo}}^{-1}. \tag{14}$$

In the latter expression,  $\mathbb{I}$  is the fourth order identity tensor w.r.t. to symmetric second rank tensors,  $\mathbb{S}_{\text{Esh}}$  is the Eshelby tensor,  $\mathbb{C}^{(g)}$  is the elastic stiffness tensor for grain number  $g$  and

$$\mathbb{L}_C^* = \mathbb{C}_{\text{Homo}} : (\mathbb{I} - \mathbb{S}_{\text{Esh}}). \quad (15)$$

The  $\boldsymbol{\beta}^{(g)}$  variables are obtained by integrating time-independent nonlinear evolution equations reminiscent of the nonlinear kinematic hardening rule:

$$\dot{\boldsymbol{\beta}}^{(g)} = \dot{\mathbf{e}}_p^{(g)} - \mathbb{D} : \boldsymbol{\beta}^{(g)} \|\dot{\mathbf{e}}_p^{(g)}\|. \quad (16)$$

These variables are initialized at  $\mathbf{0}$  in the present work. The plastic strain rate for each grain orientation  $g$  is computed as

$$\dot{\mathbf{e}}_p^{(g)} = \sum_{s \in S} \dot{\gamma}_s^{(g)} \{\mathbf{c}_m^{(g)} \otimes \mathbf{c}_n^{(g)}\}. \quad (17)$$

The Equation (16) involves a constant phenomenological tensor  $\mathbb{D}$  whose components must be calibrated. They are determined by comparing the model responses between  $\beta$ -model and a reference full-field FEM simulation of a polycrystalline aggregate following the strategy depicted in [36]. The effective accommodation variable  $\boldsymbol{\beta}$  is given by [25, 37]:

$$\boldsymbol{\beta} = \sum_g f_{(g)} \mathbb{L}_C^{*-1} : \mathbb{B}^{(g)} : \mathbb{L}_C^* : \boldsymbol{\beta}^{(g)}. \quad (18)$$

The macroscopic plastic strain  $\mathbf{e}^p$  generally deviates from the average plastic strain over all grain orientations by the following contribution:

$$\mathbf{e}^p = \sum_g f_{(g)} \mathbf{e}_p^{(g)} + \sum_g f_{(g)} [\mathbb{C}^{(g)-1} : \mathbb{B}^{(g)} : \mathbb{L}_C^* : (\boldsymbol{\beta} - \boldsymbol{\beta}^{(g)})]. \quad (19)$$

Depending on the choice of  $\mathbb{D}$ , the  $\beta$ -model can reproduce the response of the Kröner model or other self-consistent schemes better accounting for elasto-plastic accommodation of the grains than the usual Taylor model [18].

### 3. Assessment of the pencil glide model for single crystals

#### 3.1. Validation: comparison with Mandel's original scheme

The formulation of crystal plasticity using two local objective frames will be compared with Mandel's model [29] which is based on the multiplicative elastic-plastic decomposition of the deformation gradient. The comparison is made for simple shear  $\mathbf{F} = \mathbf{I} + \gamma \mathbf{e}_1 \otimes \mathbf{e}_2$ , with prescribed overall shear  $\gamma$ . According to Mandel's theory, the Mandel stress tensor is used to compute the resolved shear stress on each slip system whereas the present theory makes use of the corotational stress. Due to the fact that elastic strains in metals generally remain small, no significant discrepancy is expected. The initial orientation of the crystal is  $\mathbf{e}_1 = [100]$  and  $\mathbf{e}_2 = [010]$ . These simulations are conducted in the absence of strain hardening with a constant critical resolved shear stress  $\tau_0$ , and considering 12 slip systems  $\{110\}\langle 111 \rangle$ . It can be checked from Figure 1 that the Cauchy stress components predicted by the Mandel and corotational models are identical.

The "fish-like" oscillations of the stresses observed in Figure 1 for this orientation of a f.c.c. single crystal under simple shear were discussed in [21, 38]. It is of interest to consider the response of b.c.c. crystals to the same loading conditions. Figure 2 provides three Cauchy stress components for three slip system families, namely 12 slip systems  $\{110\}\langle 111 \rangle$ , 24 slip systems  $\{110\} + \{112\} + \{123\}$  or 4 pencil glide mechanisms. We have found that the response of 12 b.c.c. slip systems, see Figure 1, is the same as in the f.c.c. case. The consideration of 24 slip systems leads to a similar periodic response with slightly lower stress values. The lower envelope of these curves is obtained using the pencil glide model. In all cases, the rotation rate of the lattice is  $-\dot{\gamma}/2$ , i.e. the

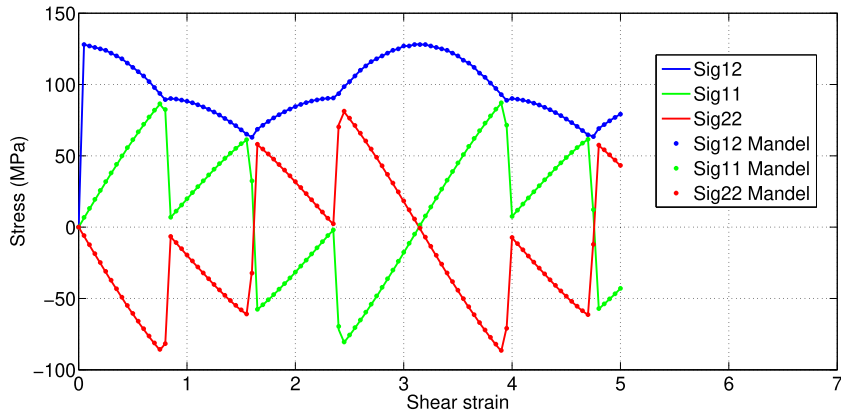


**Figure 1.** Simple glide test for a single crystal endowed with 12 slip systems  $\{110\}\langle 111\rangle$ : stress responses of the Mandel and corotational single crystal models.

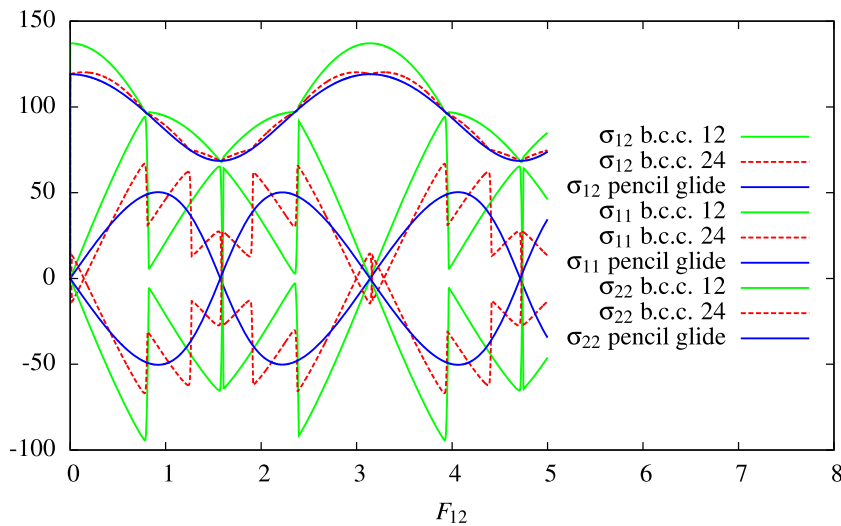


**Figure 2.** Simple glide test for a b.c.c. single crystal endowed with 12 slip systems  $\{110\}\langle 111\rangle$ , 24 slip systems  $\{110\} + \{112\} + \{123\}$  or pencil glide: stress components (MPa) computed using the single crystal model based on local objective frames, with  $r_0 = 50$  MPa, in the absence of hardening.

spin of the corotational frame. This is a remarkable feature of simple shear for ideally oriented single crystals.

### 3.2. Tension of $\alpha$ -iron single crystals

The relevance of the Schmid law is well-known for many f.c.c. crystals deforming by slip on  $\{111\}$  planes at low and intermediate temperatures. In the case of b.c.c. metals, in particular  $\alpha$ -iron at room temperature, the situation is more complicated since multiple slip planes are available, namely  $\{110\}$  and  $\{112\}$ , see Table 1. Several experiments [39, 40] have highlighted the fact that thermal effects are still at play. Slip planes  $\{123\}$  are also possible for the accommodation of plastic strain [41]. Screw dislocations gliding in  $\{110\}$  slip planes and all dislocations gliding



**Table 1.** The slip planes in b.c.c. crystals, with notations from [45, 46]

Notation	Plane	b	Notation	Plane	b
2A	(0 $\bar{1}$ 1)	$[\bar{1}11]$	6'A	(1 $\bar{1}$ 2)T	$[\bar{1}11]$
3A	(101)	$[\bar{1}11]$	2''A	(211)AT	$[\bar{1}11]$
6A	(110)	$[\bar{1}11]$	3'A	(12 $\bar{1}$ )T	$[\bar{1}11]$
2B	(0 $\bar{1}$ 1)	[111]	4''B	(1 $\bar{2}$ 1)AT	[111]
5B	( $\bar{1}$ 10)	[111]	2'B	(2 $\bar{1}$ 1)T	[111]
4B	( $\bar{1}$ 01)	[111]	5''B	(11 $\bar{2}$ )AT	[111]
1C	(011)	$[\bar{1}\bar{1}1]$	3''C	( $\bar{1}$ 21)AT	$[\bar{1}\bar{1}1]$
5C	( $\bar{1}$ 10)	$[\bar{1}\bar{1}1]$	5'C	(112)T	$[\bar{1}\bar{1}1]$
3C	(101)	$[\bar{1}\bar{1}1]$	1''C	(2 $\bar{1}$ 1)AT	$[\bar{1}\bar{1}1]$
1D	(011)	$[\bar{1}\bar{1}1]$	6'D	( $\bar{1}$ 12)T	$[\bar{1}\bar{1}1]$
4D	( $\bar{1}$ 01)	$[\bar{1}\bar{1}1]$	1''D	(21 $\bar{1}$ )AT	$[\bar{1}\bar{1}1]$
6D	(110)	$[\bar{1}\bar{1}1]$	4'D	( $\bar{1}$ 2 $\bar{1}$ )T	$[\bar{1}\bar{1}1]$

**Table 2.** Chemical elements in ARMCO® commercial iron (% weight), according to [3]

C	Mo	Si	P	S	Ti	Cr	Mn	Cu	Ni	Al	N	Va	Sn	Pb
0.0026	0.001	0.004	0.002	0.0047		0.016	0.080	0.009	0.011	0.002	0.006		0.002	

in  $\{112\}$  planes experience an energy barrier to overcome lattice friction [42, 43]. Besides, cross-slip in iron is easier owing to the dislocation compact core in b.c.c. crystals [44]. The existence of multiple cross-slip planes leads to the formation of wavy slip lines characterizing the pencil glide.

The objective of this section is to compare the description of the tensile behaviour of  $\alpha$ -iron single crystals by crystal plasticity models involving either all slip systems of Table 1 or only 4 pencil glide systems. The results of experiments with ARMCO® iron that contains impurities reported in Table 2 are taken from [3]. The dimensions of the matrix  $h^{sl}$  for b.c.c. materials is usually  $12 \times 12$  considering only one family of slip systems, but in the case of  $\alpha$ -iron, the dimensions is  $24 \times 24$ . The difficulty is that the interaction matrix required at least 17 independent coefficients, as summarized in Table 3. Some of them could be predicted by Dislocation Dynamics simulations [47–49] but many are essentially unknown. Values taken from the works [46, 50, 51] are used in the sequel.

In contrast, the pencil glide model requires a  $4 \times 4$  interaction matrix and only two parameters must be given to define this matrix, see Table 4. Calibration of these parameters is performed in order to obtain closest agreement with experimental curves.

The material parameters of both models are reported in Table 5. The power law value  $n = 20$  and low  $K$  value ensure rate-independence of the results for the considered range of strain rates.

Initially, the crystallographic axes ( $X_1$ ,  $X_2$ ,  $X_3$ ) of the samples coincide with the axes of the sample frame, labelled N, S and L to specify the directions normal to the sample observed surface, the sample side face and the sample loaded face, respectively. Tensile loading is applied along axis  $X_3$  (parallel with L). During the test, the axial material fibers remain parallel to the loading axis, which means that  $F_{13} = F_{23} = 0$ . In compression along axis  $X_3$ , material planes normal to  $X_3$  are assumed to remain parallel, leading to the conditions  $F_{31} = F_{32} = 0$ . A third condition is that the rotation with respect to axis  $X_3$  vanishes, which leads to  $F_{12} = F_{21}$  for both tension and compression.

**Table 3.** The interaction matrix in b.c.c. single crystals using {110} + {112} slip planes and the associated parameter values used for  $\alpha$ -iron. The notations and parameters values are taken from [46, 50]

	2A	3A	6A	2B	4B	5B	1C	3C	5C	1D	4D	6D	2'A	3'A	6'A	2'B	4'B	5'B	1'C	3'C	5'C	1'D	4'D	6'D
2A	DP	$\Omega_1$	$\Omega_1$	CP	B1	B1	A	B1	C	A	C	B1	$\Omega_2$	$\Omega_3$	$\Omega_3$	B2	B3	B3	D	E	F	D	F	E
3A		DP	$\Omega_1$		B1	A	C	B1	CP	B1	C	A	B1	$\Omega_2$	$\Omega_3$	E	D	F	B3	B2	B3	F	D	E
6A			DP		B1	C	A	C	B1	A	B1	B1	CP		$\Omega_2$	E	F	D	F	E	D	B3	B3	B2
2B				DP	$\Omega_1$	$\Omega_1$	A	C	B1	A	B1	C				$\Omega_2$	$\Omega_3$	$\Omega_3$	D	F	E	D	E	F
4B					DP	$\Omega_1$	C	A	B1	B1	CP	B1				$\Omega_2$	$\Omega_3$	$\Omega_3$	F	D	E	B3	B2	B3
5B						DP	B1	B1	CP	C	B1	A					$\Omega_2$	B3	B3	B2	F	E	D	
1C							DP	$\Omega_1$	$\Omega_1$	CP	B1	B1				$\Omega_2$	$\Omega_3$	$\Omega_3$	$\Omega_3$	$\Omega_3$	B2	B3	B3	
3C								DP	$\Omega_1$	B1	A	C								$\Omega_2$	$\Omega_3$	E	D	F
5C									DP	B1	C	A									$\Omega_2$	E	F	D
1D										DP	$\Omega_1$	$\Omega_1$										$\Omega_2$	$\Omega_3$	$\Omega_3$
4D											DP	$\Omega_1$											$\Omega_2$	$\Omega_3$
6D												DP												$\Omega_2$
2'A													DP	$\Omega_1$	$\Omega_1$	G	I	I	H	I	J	H	J	I
3'A														DP	$\Omega_1$	I	H	J	I	G	I	J	H	I
6'A															DP	I	J	H	J	I	H	I	I	G
2'B																DP	$\Omega_1$	$\Omega_1$	H	J	I	H	I	J
4'B																	DP	$\Omega_1$	J	H	I	I	G	I
5'B																		DP	I	I	G	J	I	H
1'C																			DP	$\Omega_1$	$\Omega_1$	G	I	I
3'C																				DP	$\Omega_1$	I	H	J
5'C																					DP	I	J	H
1'D																						DP	$\Omega_1$	$\Omega_1$
4'D																							DP	$\Omega_1$
6'D																								DP

DP = 0.07	CP = 0.07	$\Omega = 0.7$	B1 = 0.08	A = 0.14	C = 0.07	B2 = B3 = 0.1	E = 0.08	D = F = 0.11	G = H = J = 0.09	I = 0.08
-----------	-----------	----------------	-----------	----------	----------	---------------	----------	--------------	------------------	----------

**Table 4.** The interaction matrix in b.c.c. crystals using pencil glide, where  $H1 = 0.07$  and  $H2 = 0.09$  as found in the present work

	[111]	$\bar{1}\bar{1}\bar{1}$	$\bar{1}\bar{1}\bar{1}$	$\bar{1}\bar{1}\bar{1}$
[111]	H1	H2	H2	H2
$\bar{1}\bar{1}\bar{1}$		H1	H2	H2
$\bar{1}\bar{1}\bar{1}$			H1	H2
$\bar{1}\bar{1}\bar{1}$				H1

**Table 5.** Material parameters used for both pencil glide and {110}<111> + {112}<111> single crystal models

$C_{11} = 284$ GPa	$C_{12} = 149$ GPa	$C_{44} = 105$ GPa
$r_0 = 27$ MPa	$Q = 1285$ MPa	$b = 1.5$
$n = 20$	$K = 5$ MPa <sup>1/n</sup>	

Simulations are presented for 5 distinct single crystal orientations:

- *Orientation 1 (Figure 3a):* For this orientation in the centre of the reference triangle, the primary active slip system leads to a rotation of the L axis towards the [111] slip direction without activation of the secondary  $(\bar{1}01)[111]$  slip system.
- *Orientation 2 (Figure 3b):* Although the initial orientation for this case is close to a boundary  $[001] - [011]$ , and although the secondary traces do not differ much from those of the primary system, the measured rotation of the L axis towards the [111] slip direction provides unambiguous evidence of single slip even in the overshoot regime.

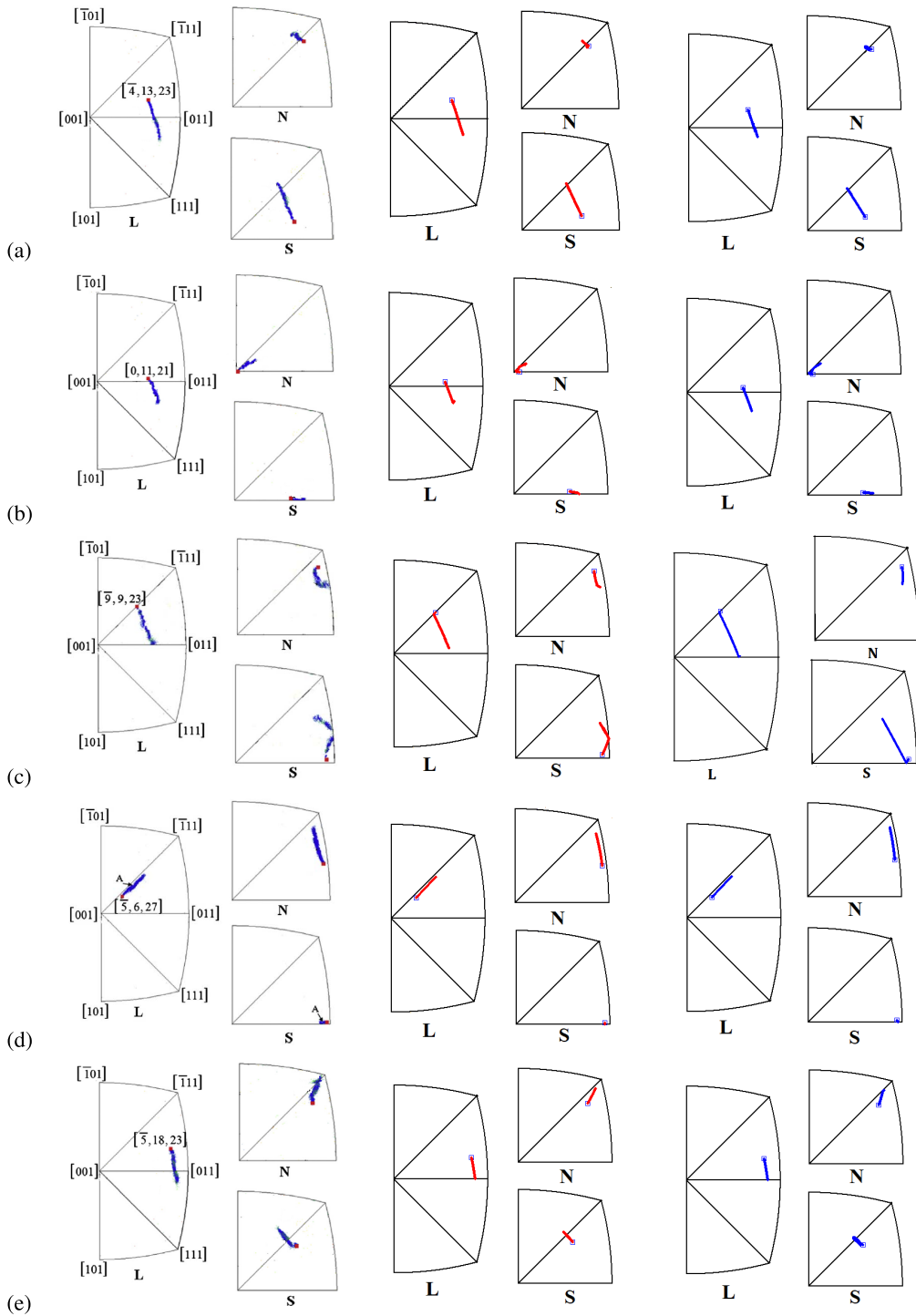


**Figure 3.** Rotations of the three axes of the sample measured by EBSD (left), and simulated rotations of the three sample axes: (middle)  $\{110\} + \{112\}$  slip systems, (right) pencil glide. The initial orientation is marked by a square symbol.

This rotation of the L axis indicates that the primary system is  $(\bar{1}01)[111]$ , which has initially a slightly higher Schmid factor. The reported measured rotations of the N and S axes also correspond with the simulated ones.

- *Orientation 3 (Figure 3c)*: This orientation lies on the boundary  $[001] - [\bar{1}11]$ : the two equally loaded  $\{110\}$  systems were found to activate in spatially separated parts of the sample with dense and straight slip lines. Then one of the two systems rapidly takes over and single slip mainly takes place for the rest of the strain path in most of the sample volume, as assessed by the lattice rotation. The lattice rotation predicted by the pencil glide model displays some discrepancy with experimental results. The reason is that it allows here for only one slip system. The interaction between 2  $\{110\}$  systems is a junction, and the corresponding coefficient in the interaction matrix has the same value as the self-hardening, however these coefficients are different when using the pencil glide model.
- *Orientation 4 (Figure 3d)*: This orientation is situated close to the corner of the domain where the  $(1\bar{1}2)[\bar{1}11]$  system has the highest Schmid factor. At the corner, two other slip systems of the  $\{110\}$  type have equal Schmid factors. The rotation of the L axis was found to be towards the  $[\bar{1}11]$  slip direction, which confirmed the activation of the  $(1\bar{1}2)[\bar{1}11]$  slip system, with good agreement between both models.
- *Orientation 5 (Figure 3e)*: The highest Schmid factor for this orientation is for the  $(\bar{2}11)[111]$  system, in competition with the collinear  $(\bar{1}01)[111]$  slip system. However, the Schmid factor ratio is initially 5% higher in favour of the  $\{112\}$  system type, with good agreement between both models.

Figure 4a shows the experimental stress-strain curves for  $\alpha$ -iron at ambient temperature. It can be seen that the hardening modulus for single slip systems  $\{110\}$  and  $\{112\}$  are different. The tensile tests performed have also reported the dissymmetric occurrence of  $\{112\}$  slip for orientations near the boundaries of the standard triangle (near direction  $[001]$  for twinning direction, and near direction  $[011]$  for anti-twinning direction). The value of the hardening modulus for the systems  $\{112\}$ AT (activated in anti-twinning direction) is greater than for the systems  $\{110\}$ , and the hardening modulus for the systems  $\{110\}$  is larger than the systems  $\{112\}$ T (activated in twinning direction). When multiple slip systems are active, the hardening moduli are larger than for single slip even if the activation of multiple slip systems is not stable.

Corresponding tensile curves for the full single crystal and the reduced pencil glide models are provided in Figure 4b. It is found that the pencil glide model predicts the tensile response of  $\alpha$ -iron as accurately as classical crystal plasticity with 24 slip systems. There is little difference even if the same parameters are used for both models (see Table 5) except the interaction matrix which differs for both models (see Tables 3 and 4 respectively). The simulated curves are essentially in good agreement with experimental results. Lattice rotation is also well-predicted in general. Some discrepancies can be observed in the stress-strain curves that can be attributed to the fact that we did not account for the dissymmetric activation of slip systems  $\{112\}$ . This can be done but it is out of the scope of the present paper.

## 4. Assessment of the pencil glide model for $\alpha$ -iron polycrystals

### 4.1. Identification of scale bridging parameters

In the  $\beta$ -model,  $\mathbb{D}$  denotes a fourth order phenomenological constant tensor to be calibrated. Its components are identified by comparing the model responses between the  $\beta$ -model and

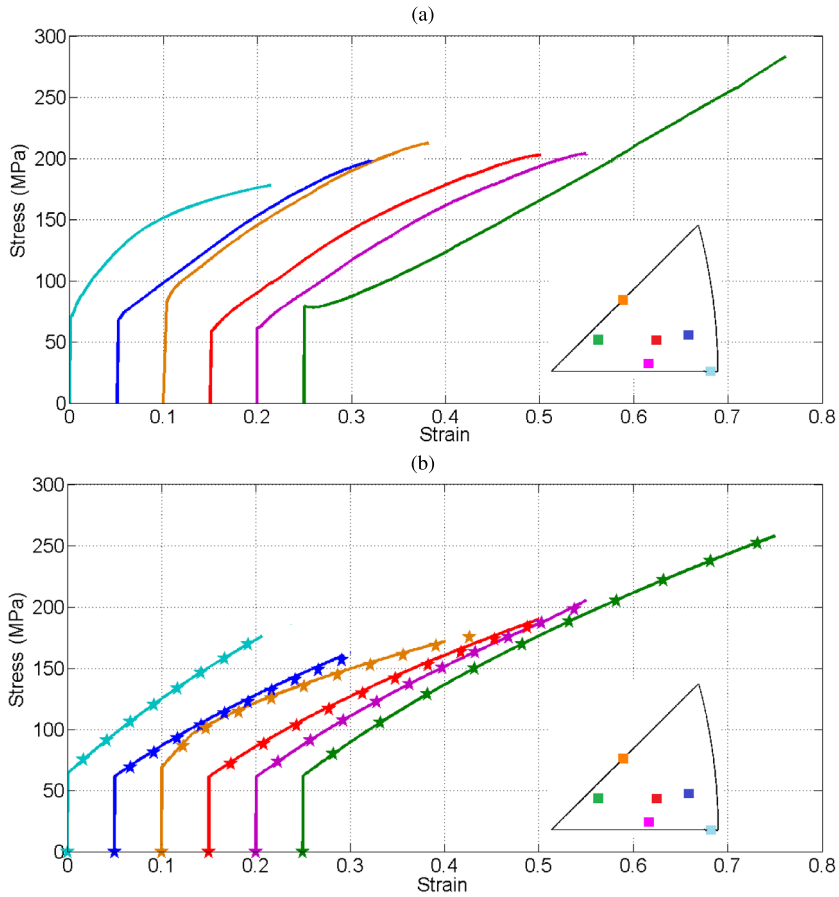


**Figure 4.** True stress–true strain curves for 6 single crystal orientations: (a) experimental results, (b) simulation results: {110} + {112} slip systems (continuous line), pencil glide model (stars). The corresponding initial orientations are indicated in the standard triangle by a square of the same color.

reference full-field simulations. In this work, the following form is considered for  $\mathbb{D}$ , as proposed by [22, 23] for the anisotropic elasto-plastic properties of multi-axial aggregates:

$$[\mathbb{D}\beta^{(g)}] = \begin{bmatrix} D_{11} & D_{12} & D_{23} & & & & \\ D_{12} & D_{33} & D_{23} & & & & \\ D_{23} & D_{23} & D_{33} & & & & \\ & & & D_{44} & & & \\ & & & & D_{55} & & \\ & & & & & D_{55} & \\ & & & & & & \end{bmatrix} \begin{bmatrix} \beta_{11}^{(g)} \\ \beta_{22}^{(g)} \\ \beta_{33}^{(g)} \\ \sqrt{2}\beta_{12}^{(g)} \\ \sqrt{2}\beta_{23}^{(g)} \\ \sqrt{2}\beta_{31}^{(g)} \end{bmatrix} \tag{20}$$

where the components are given in the material frame  $(X_1, X_2, X_3)$  of the metal sample, assuming transverse isotropy for the textures considered in the following simulations. The  $\beta$  variables

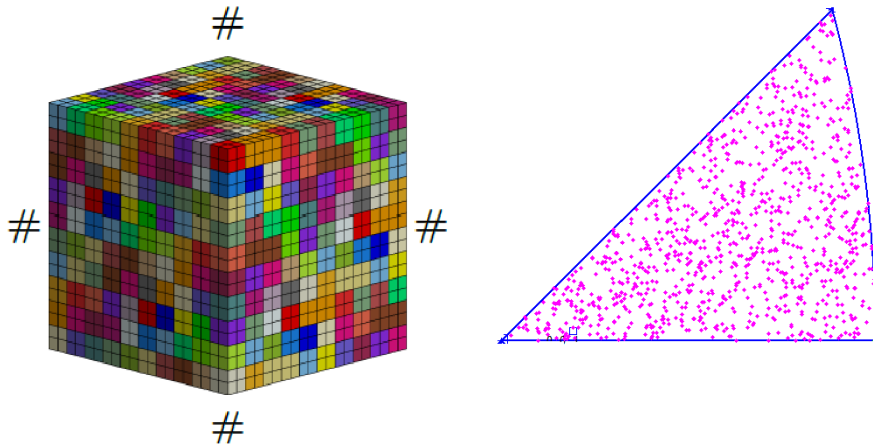


**Figure 5.** Meshes for full-field finite element model (FEM), and initially isotropic 1000 grain orientation distribution. Each grain contains eight finite elements with quadratic interpolation and reduced integration.

**Table 6.** Identified parameters for the  $\beta$ -model

$$\overline{D_{11} = 10 \quad D_{12} = 1 \quad D_{23} = 1 \quad D_{44} = 5 \quad D_{55} = 5}$$

are assumed to be deviatoric, i.e.  $\text{trace}(\boldsymbol{\beta}^{(g)}) = 0$ , so that the following additional condition is enforced [22]:

$$D_{11} = D_{33} + D_{23} - D_{12}. \quad (21)$$

We keep five independent coefficients  $D_{ij}$  to be determined by an identification procedure. With this form of  $\mathbb{D}$ , it will be found that  $\beta$ -model predictions fit satisfactorily the results obtained by the full-field FEM reference for the anisotropic behaviour of polycrystalline aggregates. For that purpose, an elementary volume  $V$  made of a parallelepipedic tessellation of  $(10 \times 10 \times 10)$  1000 grains is considered, see Figure 5. Periodic boundary conditions are prescribed. The parameters  $D_{11}$ ,  $D_{12}$ ,  $D_{23}$  can be calibrated from a tensile test on this volume, whereas  $D_{44}$  and  $D_{55}$  are obtained from shear tests. An isotropic distribution of 1000 orientations is considered for the simulation and distributed randomly among the square grains of Figure 5. Almost isotropic  $\mathbb{C}_{\text{Homo}}$  and  $\mathbb{D}$  tensors are obtained. The found parameters for  $\mathbb{D}$  are given in Table 6. The same set of parameters is found to provide a correct fit for both  $\{110\} + \{112\}$  and pencil glide models, as illustrated in Figure 6.

The FEM simulations were performed twice for each loading: one simulation taking the 24 slip systems into account in each grain, and one with the 4 pencil glide systems. The predicted yield stresses are very close to both models but the pencil glide model predicts significantly lower hardening. This is due to the fact that the applied resolved shear stresses on the pencil glide systems are greater than on the  $\{110\} + \{112\}$  slip systems. Accordingly, the pencil glide model provides the lowest stress-strain relation possible due to an increase in degrees of freedom for the selection of the slip plane. Furthermore, the larger number of available slip systems in the reference model leads to more interactions via the interaction matrix and associated additional hardening. The mean field  $\beta$ -model is found to overestimate hardening compared with the reference FEM. It has been checked that different  $D_{ij}$  combinations will not reduce this deviation. It is noted that the same material parameters are used for the single crystal model in the FEM and mean field simulations. Better agreement can be reached using more

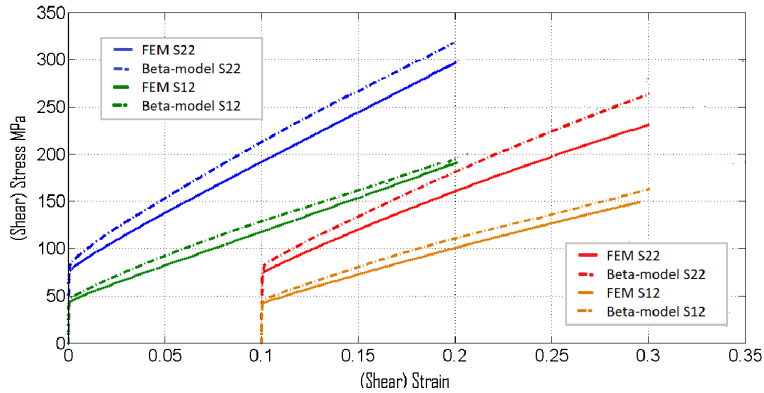


**Figure 6.** Tensile (called S22) and shear (called S12) curves for a 1000-grain polycrystal according to the full field (continuous line) and mean field (dashed lines) models: blue and green curves for the  $\{110\} + \{112\}$  crystal plasticity model; red and orange curves for the pencil glide model. Stress (resp. strain) values correspond to the Cauchy stress components  $\sigma_{22}$  and  $\sigma_{12}$  (resp.  $F_{22} - 1$  and  $F_{12}$  prescribed components).

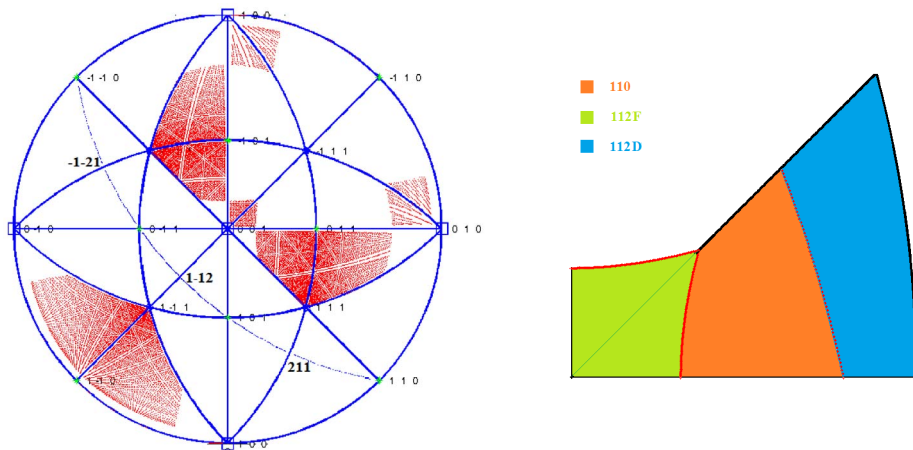


**Figure 7.** Activation zone for the slip direction  $[\bar{1}11]$  according to the pencil glide model (left) and activation zones for slip planes families according to Schmid's law (right).

sophisticated evolution equations for the  $\beta$ -variables [24] but this is not the focus of the present work. As such, these results demonstrate that the fast computational  $\beta$ -model is an efficient homogenization tool correctly reflecting the responses of full-field and mean field models at least for the considered loading conditions.

#### 4.2. Tensile test

Tensile tests have been performed for the mean field models with 352 random orientations. The result is a combination of all the examples of the previous section. In simple tension of single crystals, single slip leads to rotation of the tensile axis towards a  $\langle 111 \rangle$  slip direction. In the case of polycrystals, because of the deviation of stress and strain from uniaxial tension, the phenomenon is more subtle. But the average rotation of grains can be similar. Figure 7 shows the activated zone associated with slip direction  $[\bar{1}11]$  for pencil glide (left) and the activated zone in standard

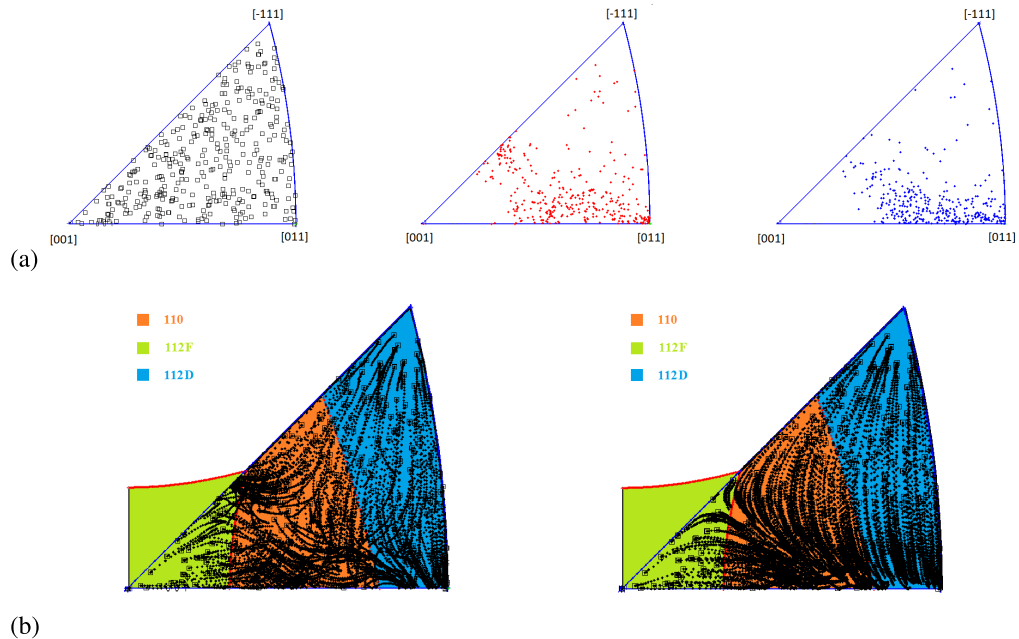


**Figure 8.** (a) Initial isotropic (left) and final grain orientations after 50% tensile straining using  $\{110\} + \{112\}$  slip systems (middle) and pencil glide systems (right). (b) Trajectories of individual grains in the standard triangle in tension using  $\{110\} + \{112\}$  slip systems (left) and pencil glide systems (right).

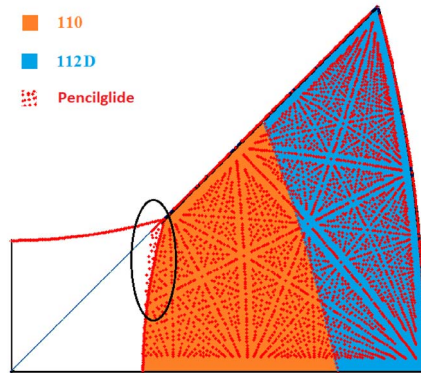
triangle by Schmid's law. The lattice rotation will be different if the initial orientation lies in the green or orange zones. More complex orientation paths are observed for initial orientations close to boundaries of the standard triangle.

Figure 8a shows the initial and final grain orientations as predicted by the crystal plasticity model using  $\{110\} + \{112\}$  slips systems or pencil glide systems. The tensile axis at the end of the two simulations after 50% strain is close to the boundary  $[001] - [011]$ , and the zone  $[\bar{1}12] - [111]$ . The pencil glide predicts similar results as the  $\{110\} + \{112\}$  model, however with a more pronounced texture development.

Figure 8b shows the trajectories of individual grains according to both model predictions in tension. In both cases, if the tensile axis is close to  $[011] - [\bar{1}11]$ , the tensile axis will start rotating towards the slip direction  $[111]$  (with activation of  $(\bar{2}11)[111]$  slip system), as long as single slip conditions dominate. At larger deformations, a secondary slip system  $(211)[\bar{1}11]$  is activated, associated with  $[\bar{1}11]$  slip direction. The tensile axis will then turn towards  $[011]$  direction and stay there. In contrast, if the tensile axis is close to  $[001] - [\bar{1}11]$  boundary, at the beginning, double slip starts right away and the tensile axis turns down to  $[001]$  direction. When the grains reach the activation zone for  $\{110\}$  slip systems, the tensile axis turns down toward  $[111]$  direction because the  $(\bar{1}01)[111]$  slip system starts gliding.

If the initial orientation of the tensile axis is close to direction  $[001]$ , one or multiple slip systems  $\{112\}$  are activated. But this direction is not stable in tension, so that at the end the tensile axis will turn up towards slip directions  $\langle 111 \rangle$  (if the slip plane is  $(1\bar{1}2)$ , the slip direction is  $[\bar{1}11]$ ). At large deformations, the tensile axis will rotate towards the activation zone of  $\{110\}$  slip systems. Their actual activation depends on the interaction matrix and the corresponding stress value that would allow for the activation of one or 2 slip systems,  $(\bar{1}01)$  or  $(011)$ . In the case of single slip, the





**Figure 9.** Activation zone of  $\{110\} + \{112\}$  slip systems (color) and pencil glide systems (dots).

tensile axis will turn down to direction  $[111]$ . In the case of double slip, the tensile axis could remain stable at  $[\bar{1}12]$  direction. It is observed that both models provide the same results in this respect.

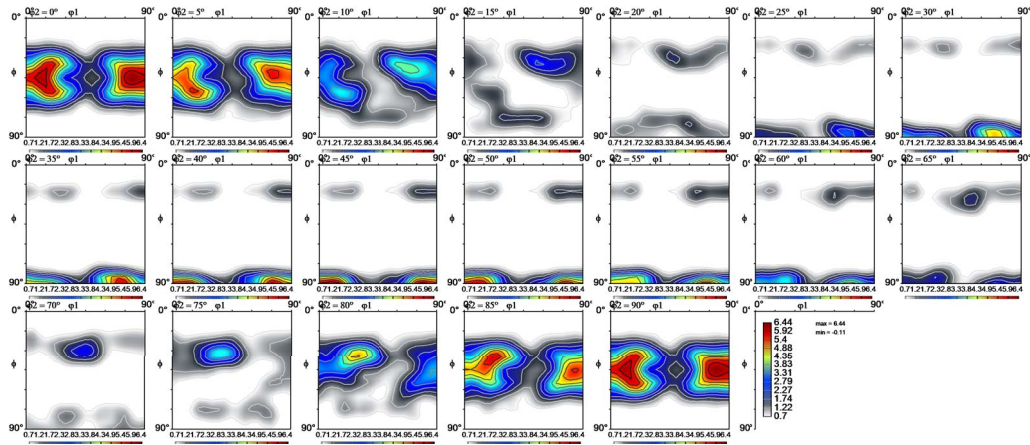
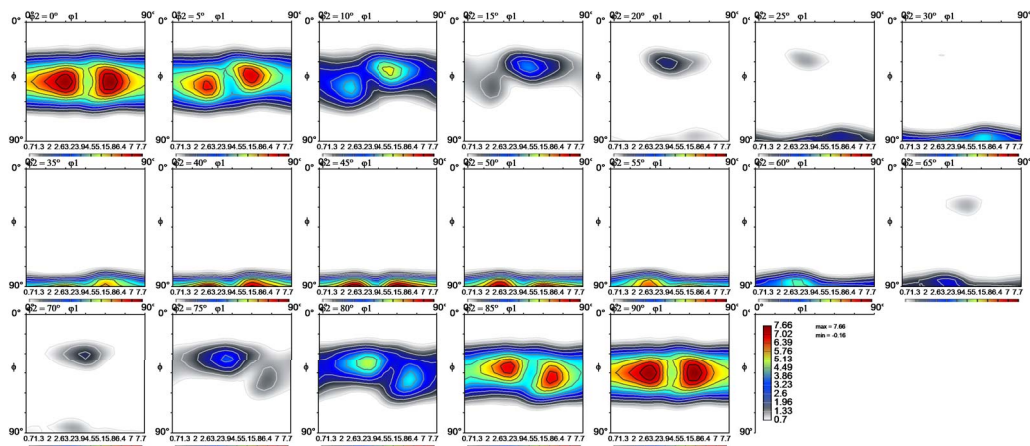
If the tensile axis lies in the central region of the standard triangle, the activated slip system family is  $\{110\}$ , and the tensile axis will rotate towards the slip direction  $[111]$ . The trajectory could pass the boundary  $[001] - [011]$ , in this case latent hardening will postpone activation of new systems. At large deformations, the secondary slip system  $(101)[\bar{1}11]$  is activated so that the tensile axis will turn up again to the slip direction  $[\bar{1}11]$ . At the end the tensile axis may stabilize at the boundary  $[001] - [011]$ . For such initial orientations, larger differences are observed between the two model predictions (Figure 8b). With pencil glide, the tensile axis will turn down to boundary  $[001] - [011]$  whereas the consideration of  $\{110\} + \{112\}$  slip systems stabilizes the tensile axis at the upper corner of the green–orange intersection due to three activated slip systems:  $(\bar{1}\bar{2})[\bar{1}11]$ ,  $(\bar{1}01)[111]$ ,  $(101)[\bar{1}11]$ .

Figure 9 shows the comparison of the activation zones for  $\{110\} + \{112\}$  slip systems associated with  $[111]$  slip direction (orange, blue) and for pencil glide associate with the same slip directions (dotted region). Only slight differences can be observed. The circled region coincides with the 3 corner zone of 3 activated slip systems:  $(\bar{1}\bar{2})[\bar{1}11]$ ,  $(\bar{1}01)[111]$ ,  $(101)[\bar{1}11]$ . More precise comparison is possible looking at the ODF maps of Figure 10. These maps are rather similar for both models, but in the case of pencil glide, the intensity of hot spots is a little higher: 7.66 compare to 6.44.

#### 4.3. Compression test

In axial compression along axis X3, assuming that material planes remain parallel to the compression plane leads to the conditions  $F_{31} = F_{32} = 0$ . The third condition is taken as the rotation  $F_{12} - F_{21} = 0$ . Figure 11 shows the initial and final orientations after 0.5 compression straining ( $F_{33} = 0.5$ ) using  $\{110\} + \{112\}$  slip systems or pencil glide systems. The compression axis of most grains at the end of both simulations is close to the boundary  $[001] - [\bar{1}11]$  and particularly in the  $[001]$  and  $[\bar{1}11]$  directions. Both models predict similar trends. It should be noted that, in tension, the slip directions of  $\{110\} + \{112\}$  slip systems and the pencil glide are the same  $\langle 111 \rangle$  but in compression, the difference between the  $\{110\} + \{112\}$  model and pencil glide can reach  $15^\circ$ .

The trajectories of individual grains are given in Figure 11b. If the compression axis is close to  $[011] - [\bar{1}11]$ , the activated slip system is  $(\bar{2}11)[111]$ , so that the compression axis will rotate

(a)  $\{110\} + \{112\}$  slip systems

(b) Pencil glide

**Figure 10.** ODF maps for 352 grains after 0.5 tensile straining according to two crystal plasticity models.

toward the slip plane normal  $[\bar{2}11]$  close to  $[\bar{1}11]$  direction. At very large deformations, the secondary slip systems  $\{112\}$  can be activated and then the compression axis remains stable in the direction  $[\bar{1}11]$ .

If the compression axis lies in the middle of the standard triangle, the active slip planes are  $\{110\}$ , and the compression axis will turn up to the slip plane  $[\bar{1}01]$ . Then when the compression axis goes close to the boundary  $[001] - [\bar{1}11]$ , the secondary slip system  $(011)[\bar{1}11]$  could be activated, leading to a slow rotation of the compression axis towards direction  $[\bar{1}11]$ . If the loading direction is at the boundary  $[001] - [011]$ , two slip systems  $\{110\}$  could be activated, then the compression axis will turn towards the  $[001]$  direction.

If the compression axis is close to  $[001]$ , the activated slip system is  $(1\bar{1}2)[\bar{1}11]$ . The compression axis turns down towards  $[\bar{1}12]$ . When it passes close to the  $[001]$  direction, multi-slip can occur and  $[001]$  will be a stable orientation.

At the end the compression axis will stay close to  $[001] - [\bar{1}11]$  zone and most probably close to the corner directions  $[001]$  or  $[\bar{1}11]$ . According to the model using  $\{110\} + \{112\}$ , the

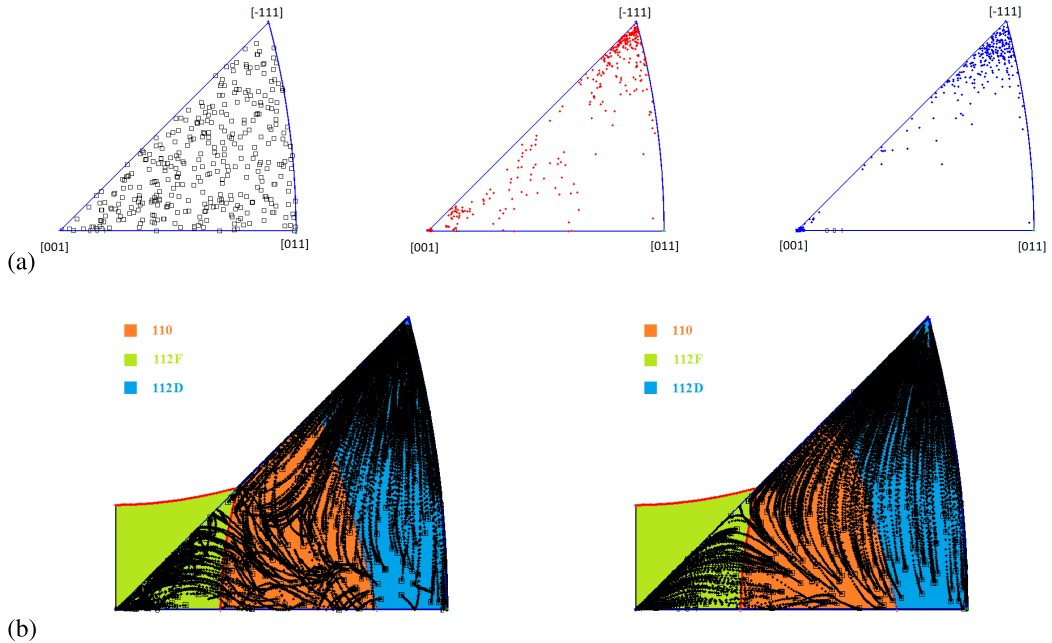


**Figure 11.** (a) Initial isotropic texture (left) and final texture after compression straining using  $\{110\} + \{112\}$  slip systems (middle) and pencil glide systems (right). (b) Trajectories of individual grains in the standard triangle during compression straining using  $\{110\} + \{112\}$  slip systems (left) and pencil glide systems (right).

compression axis could stabilize at the corner where three systems are activated:  $(\bar{1}\bar{1}2)[\bar{1}11]$ ,  $(\bar{1}01)[111]$ ,  $(010)[\bar{1}11]$ . This cannot occur when pencil glide is considered. The ODF maps of Figure 12 show that the pencil glide and  $\{110\} + \{112\}$  essentially predict the same texture in simple compression. The maximum intensity in the case of pencil glide is almost identical: 12.71 compared to 12.62.

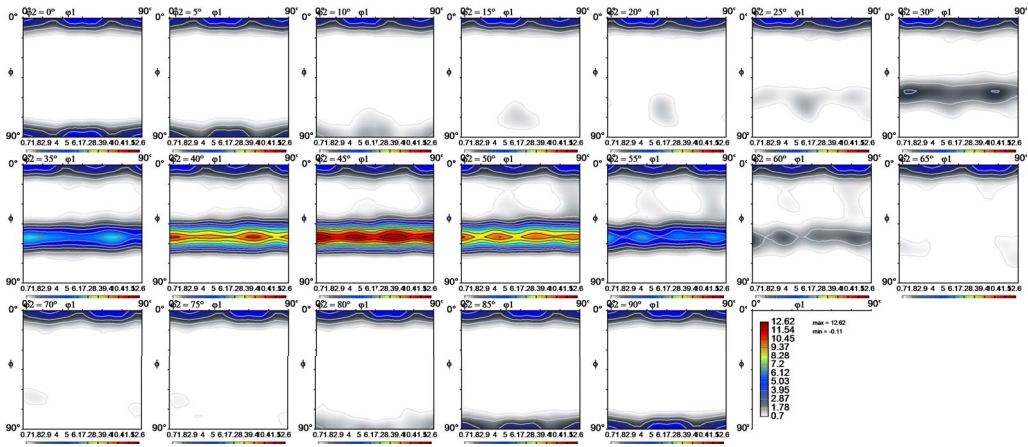
#### 4.4. Rolling

Rolling textures are crucial to evaluate the capabilities of crystal plasticity models. Rolling is simulated here by plane strain compression along axis  $X_3$ , with the plane strain direction along axis  $X_2$  (ND):  $F_{ij} = 0$  for  $i \neq j$ ,  $F_{22} = 1$ ,  $F_{33} = 1 + \epsilon$  is prescribed. The rolling direction RD is  $X_1$ .

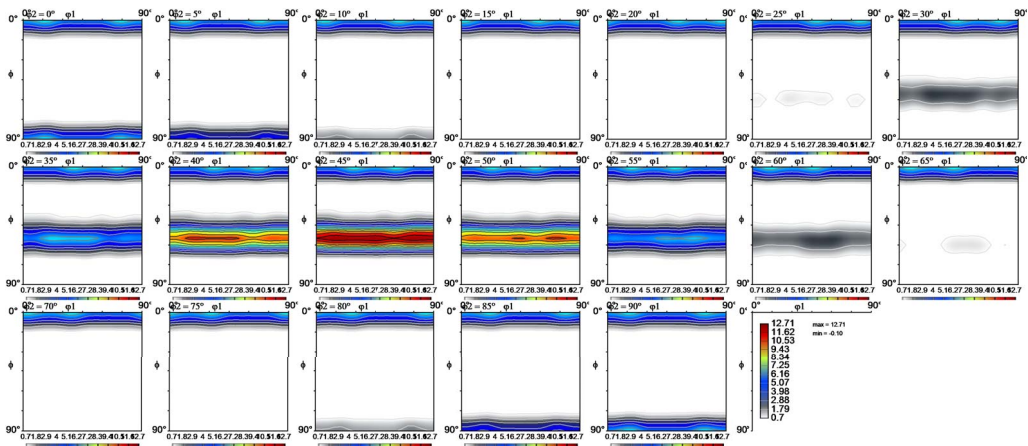
The rolling textures of b.c.c. metals are generally composed of certain orientation fibers and their main features can thus be represented in a condensed manner by plotting the orientation density along these fibers. The most important fibers and the ideal rolling texture components are described in Table 7 and illustrated in Figure 13. Figure 14 (top figure) shows the textures obtained from experiments in [52] that can be compared with the results of several crystal plasticity models.

The bottom Figure 14 presents the pole figures predicted by the Taylor model at 20% deformation. The experimental and predicted textures are similar. The main fibers like  $\alpha$  or  $\gamma$  can be observed. At small deformations the Taylor model is known to provide good predictions of rolling textures at limited strain levels. Limitations of the Taylor model are expected at large deformations.

Figure 15 displays the rolling textures as predicted by the  $\beta$ -model at 100% logarithmic strain ( $F_{33} = 0.36$ ) using the  $\{110\} + \{112\}$  slip systems and the pencil glide. The comparison shows



(a) {110} + {112} slip systems



(b) Pencil glide

**Figure 12.** ODF maps for 352 grains after 0.5 compression straining according to two crystal plasticity models.

**Table 7.** The important fibers and texture components for crystallographic textures of b.c.c., after [53, 54]

Fiber name	Fiber axis	Important texture components
$\alpha$ -fiber	{110} parallel to RD	{001}<110>, {112}<110>, {111}<110>
$\gamma$ -fiber	{110} parallel to ND	{111}<112>, {111}<110>
$\eta$ -fiber	{001} parallel to RD	{001}<100>, {011}<100>

that pencil glide leads to an increase in the intensity of texture. This result is known from other works [32]. The final textures are rather similar. However there are some differences in the development of the two fibers  $\alpha$  and  $\gamma$  between the models. Figure 16 shows the ODF sections for  $\varphi_2 = 45^\circ$  as predicted by the  $\beta$ -model using the {110} + {112} slip systems and the pencil

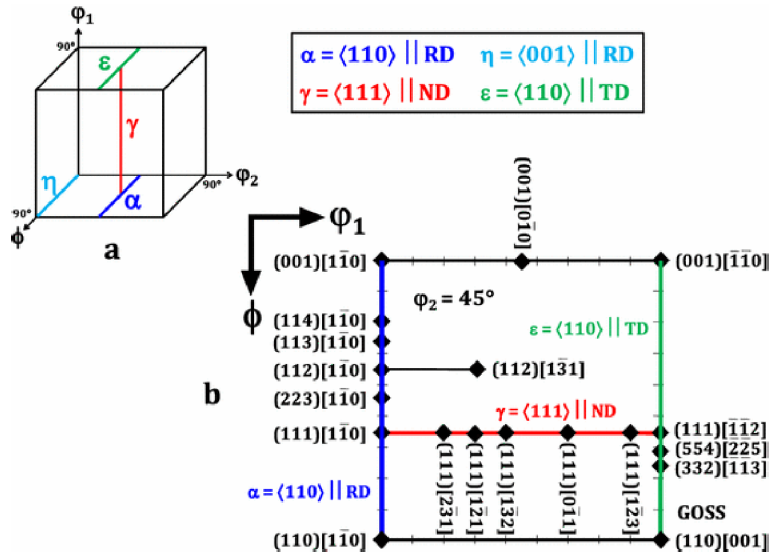


**Figure 13.** Description of  $\alpha$ -fiber and  $\gamma$ -fiber, after [55].

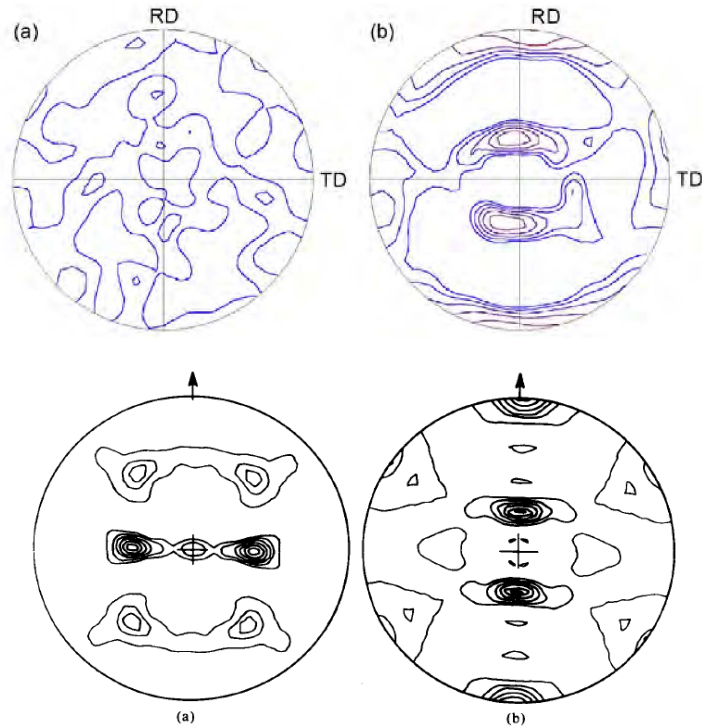
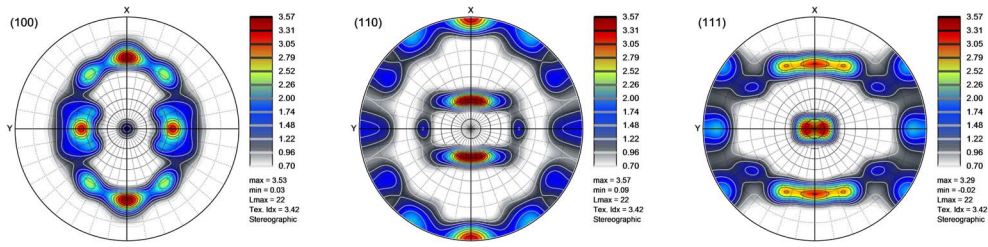
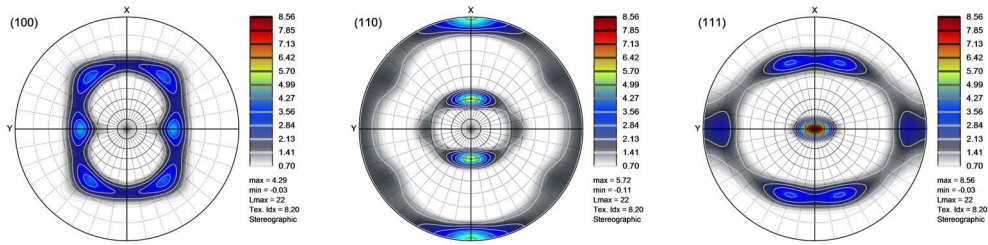


**Figure 14.** Top:  $\{110\}$  pole figures for ARMCO® iron (a) as-received; (b) after cold rolling to 64% rolling reduction [52]. Bottom: texture predicted by the Taylor model with  $\{110\} + \{112\}$  slip systems: (a)  $\{100\}$  pole figure, (b)  $\{110\}$  pole figure, after [56].

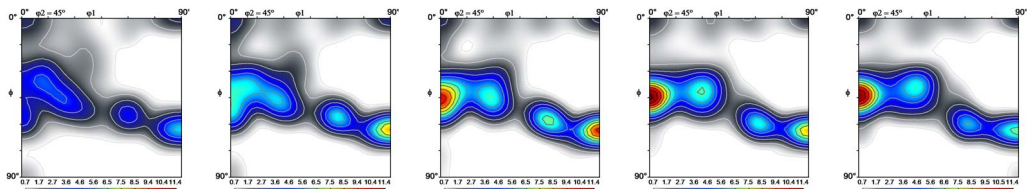


(a)  $\{110\} + \{112\}$  slip systems.

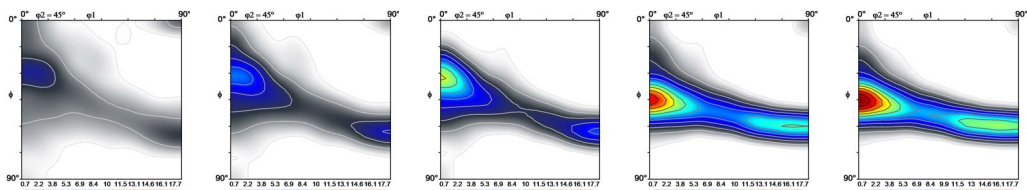


(b) Pencil glide.

**Figure 15.** Rolling pole figures predicted by the  $\beta$ -model based on two different slip mechanisms.



(a)  $\{110\} + \{112\}$  slip systems.

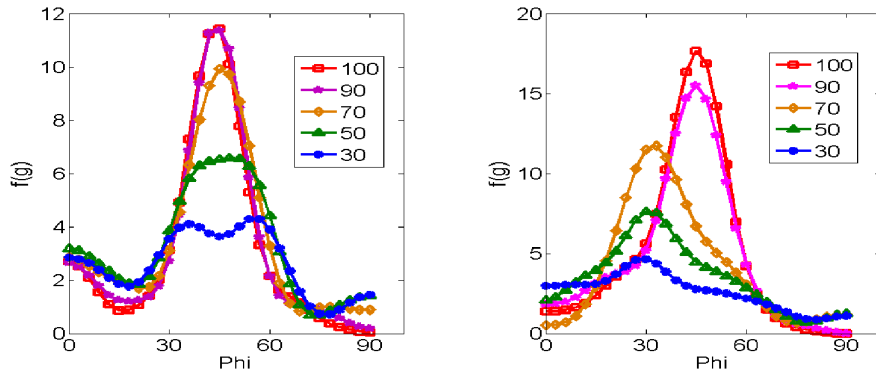


(b) Pencil glide.

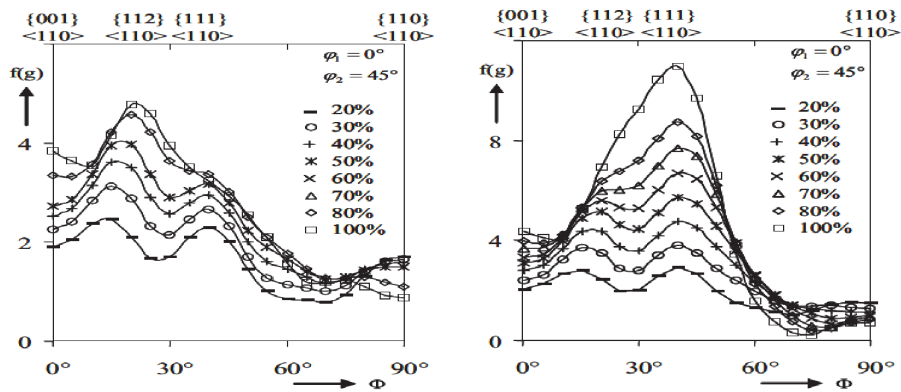
**Figure 16.** ODF section for  $\phi_2 = 45$  after 100% logarithmic rolling strain.

glide models. One can observe the distinct development of the two fibers  $\alpha$  and  $\gamma$  according to both models, see also the discussion in the ideal case in [57].

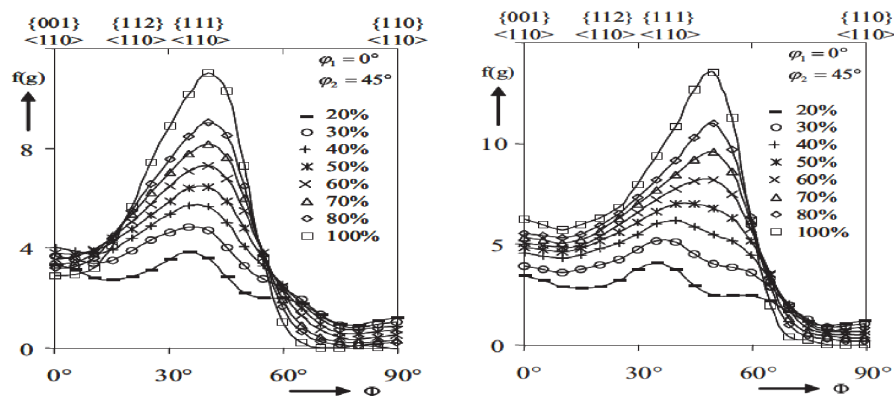
For a more accurate comparison, the evolution of the intensity of the  $\alpha$  fiber is plotted in Figure 17a. All the models predict that the  $\alpha$  fiber continuously grows with strain. The shape, the number of peaks and their location are similar for the two models considered in this work, at least after 70%. Clearly the final intensity resulting from the pencil glide mechanism is larger, 18, than considering the  $\{110\} + \{112\}$  slip systems, 12. Comparison with other models shows that the number of available slips systems controls the intensity of the fiber [59]. For instance



(a)  $\{110\} + \{112\}$  slip systems (left) and pencil glide (right)



(b)  $\{110\}$  slip systems (left) and  $\{110\} + \{112\} + \{123\}$  (right) Taylor model



(c)  $\{110\}$  slip systems (left) and  $\{110\} + \{112\} + \{123\}$  (right) VPSC model

**Figure 17.** Comparison of rolling texture fibers as predicted by (a) the  $\beta$ -model, (b) the Taylor model [58] and (c) the VPSC model, for various combinations of slip system families [58], against pencil glide.

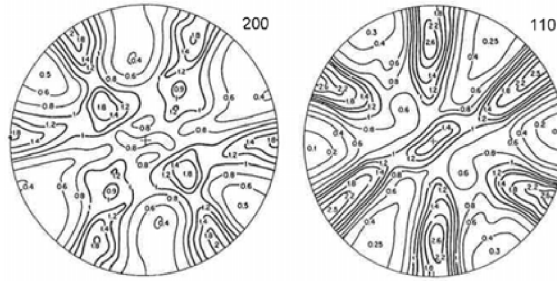


**Figure 18.** Experimental pole figures for ARMCO® iron sheared, after [61].

**Table 8.** The important fibers and texture components for crystallographic textures of b.c.c. metals, after [60]

Components	{hkl}	$\langle uvw \rangle$	$\phi_1$	$\Phi$	$\phi_2$
$D_1$	$\{\bar{1}\bar{1}1\}$	$\langle 011 \rangle$	125.26	45.0	0.0
$D_2$	$\{\bar{1}\bar{1}1\}$	$\langle 011 \rangle$	54.74	45.0	0.0
$E_1$	$\{\bar{1}\bar{1}1\}$	$\langle 121 \rangle$	270.0	35.26	45.0
$E_2$	$\{\bar{1}\bar{1}1\}$	$\langle 112 \rangle$	90.0	35.26	45.0
$F$	$\{\bar{1}00\}$	$\langle 011 \rangle$	180.0	45.0	0.0
$J_1$	$\{\bar{1}\bar{2}1\}$	$\langle 111 \rangle$	270.0	54.74	45.0
$J_2$	$\{\bar{1}\bar{1}2\}$	$\langle 111 \rangle$	90.0	54.74	45.0
$T$	$\{9\bar{1}010\}$	$\langle 15536 \rangle$	46.5	55.3	17.1

in Figure 17b, a different development of the peaks and the intensity values is observed for the Taylor model [58]. Including the  $\{123\}$  family in addition to  $\{110\} + \{112\}$  slip systems makes the Taylor prediction closer to the predictions of Figure 17a (right), with a maximal intensity of about 11 and larger peak width. After 50% strain, the  $\beta$ -model predicts a single peak whereas two peaks are observed in the Taylor simulations. The results of the  $\beta$ -model are closer to the VPSC (Viscoplastic Self-Consistent) estimates, reproduced in Figure 17c from [58], but the intensities are found to be higher. The maximum intensities according to the VPSC model for  $\{110\}$  slip systems and for  $\{110\} + \{112\} + \{123\}$  slip systems respectively are 11 and 14, instead of 12 and 18 (pencil glide). It follows that not only the number of slips systems controls the intensity but also the chosen homogenization scheme. The other parameters influencing the peak sharpness are the interaction matrix and the hardening modulus.

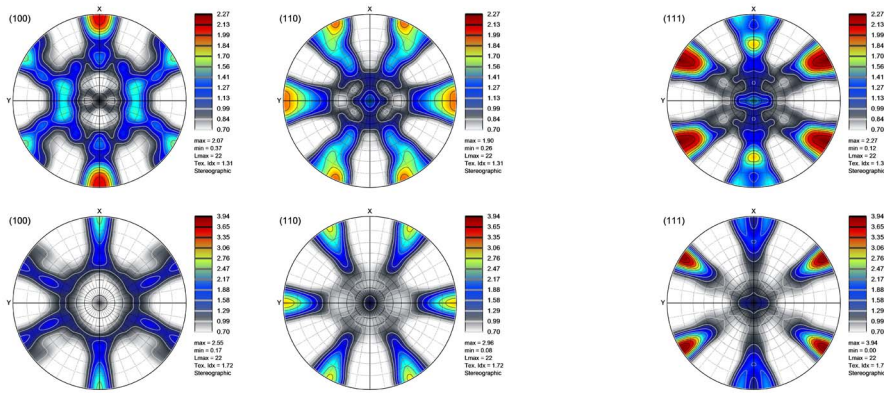
#### 4.5. Simple shear case

The simple shear test conditions correspond to a prescribed value of the component  $F_{12} = \gamma$ , whereas all other components of the deformation gradient  $\mathbf{F} - \mathbf{1}$  vanish. Experiments are often performed using torsion tests, which may not be equivalent to the simple shear considered here for simplicity. In b.c.c. materials, the crystallographic texture is composed of several main components listed in Table 8, after [60].

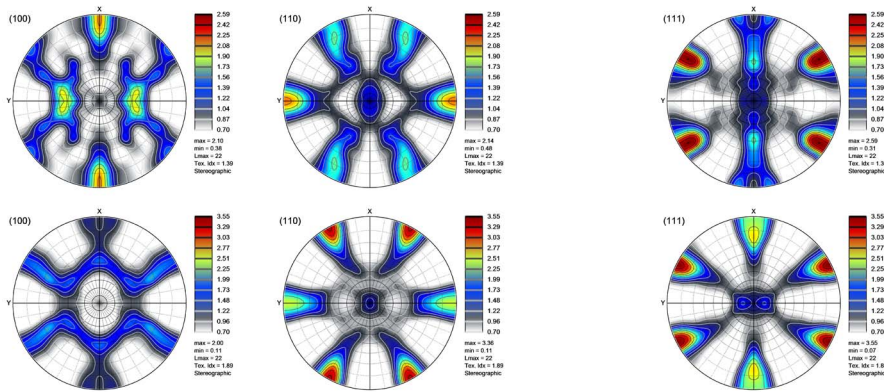
There are fewer texture evolution results under simple shear in the literature for b.c.c. metals than for f.c.c. Williams [61] tested the ARMCO® iron at room temperature, up to a shear strain of 2.1 (Figure 18). The final texture is dominated by the  $\{112\}\langle 111 \rangle$  ( $J_1, J_2$ ),  $\{110\}\langle 001 \rangle$  ( $F$ ) components.

The  $\beta$ -model provides a good estimation of the experimental results as shown in Figure 19. At  $\gamma = 1$ , there is a slight difference between the pencil glide and the  $\{110\} + \{112\}$  slip systems.

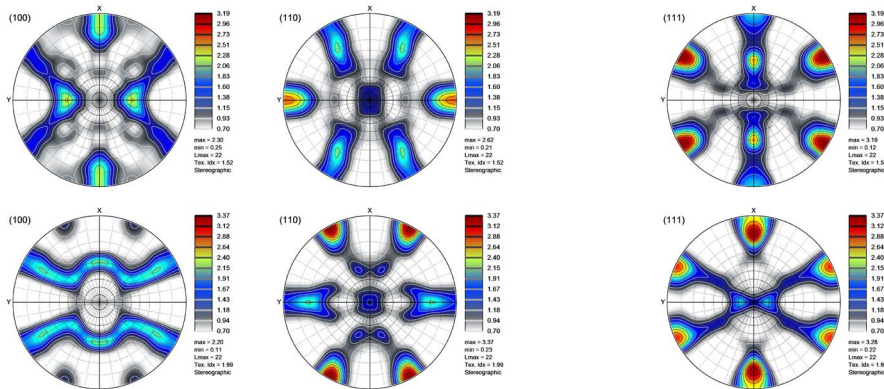




(a) Shear amount  $F_{12} = \gamma = 1$ . using  $\{110\} + \{112\}$  slip systems (top), and pencil glide (bottom)

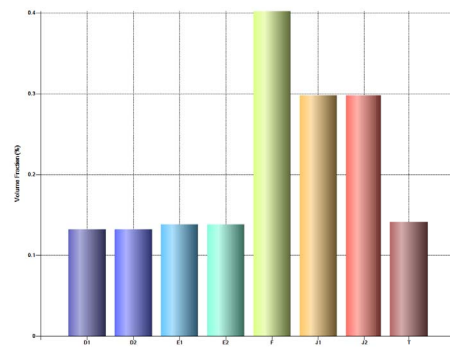
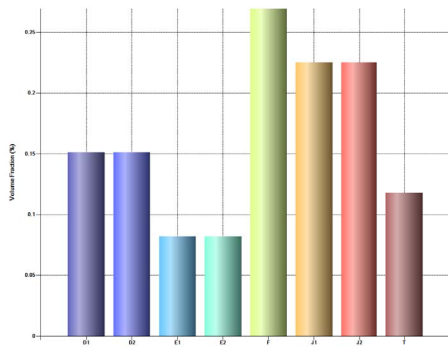


(b) Shear amount  $F_{12} = \gamma = 1.5$  using  $\{110\} + \{112\}$  slip systems (top), and pencil glide (bottom)

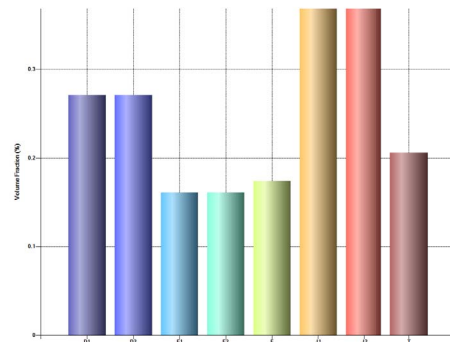
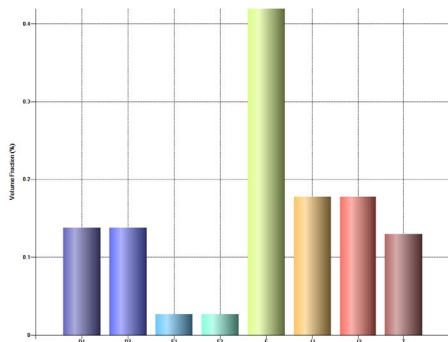


(c) Shear amount  $F_{12} = \gamma = 2.1$  using  $\{110\} + \{112\}$  slip systems (top), and pencil glide (bottom)

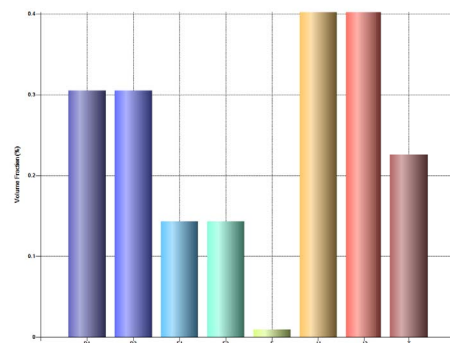
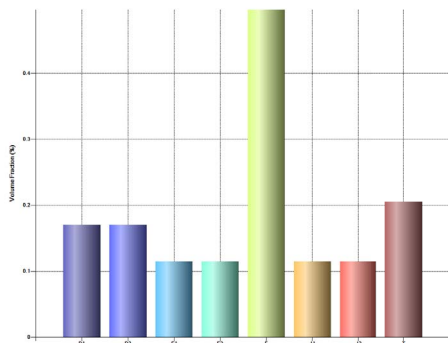
**Figure 19.** Pole figures showing the crystallographic textures induced by simple shear using the  $\beta$ -model.



(a) Shear amount  $F_{12} = \gamma = 1$  using  $\{110\} + \{112\}$  slip systems (left), and pencil glide (right)



(b) Shear amount  $F_{12} = \gamma = 1.5$  using  $\{110\} + \{112\}$  slip systems (left), and pencil glide (right)



(c) Shear amount  $F_{12} = \gamma = 2.1$  using  $\{110\} + \{112\}$  slip systems (left), and pencil glide (right)

**Figure 20.** Volume fractions of main components after simple shear according to the  $\beta$ -model.

Looking at the volume fraction of these components plotted in Figure 20a shows that the texture is dominated by the  $\{112\}\langle 111 \rangle$  (J1,J2) and  $\{110\}\langle 001 \rangle$  (F) components. But the component F is more important in the pencil glide case (volume fraction = 0.4) than in the  $\{110\} + \{112\}$  case (volume fraction = 0.26), see Figure 20a.

Increasing the shear strain  $\gamma$  leads to significant texture changes, and the pencil glide does not describe accurately the experimental results. At  $\gamma = 1.5$  the texture induced by pencil glide

is dominated by the  $\{112\}\langle 111 \rangle$  (J1,J2) components (volume fraction = 0.35) even though the F component is still present (volume fraction = 0.18). In contrast,  $\{110\} + \{112\}$  slip leads to a dominating  $\{110\}\langle 001 \rangle$  (F) component (volume fraction = 0.41) (Figure 20b).

At  $\gamma = 2.1$  the texture resulting from pencil glide is dominated by the  $\{112\}\langle 111 \rangle$  (J1,J2) components (volume fraction = 0.4) and the F component is fading away. The texture resulting from  $\{110\} + \{112\}$  slip systems is dominated only by the  $\{110\}\langle 001 \rangle$  (F) components (volume fraction = 0.5) (Figure 20c).

## 5. Discussion

Recent detailed studies on iron single crystals show that the pencil glide must be regarded as a simplified view of actual slip processes occurring on many slip planes [2, 3, 62]. In the present work we insist on the merits of the pencil glide model from the point of view of computational efficiency. In metals and alloys deforming by means of many simultaneous plasticity mechanisms like multiple slip families, twinning and martensitic transformation (like in TRIP-TWIP steels), accounting for all mechanisms leads to a dramatic increase in the number of internal variables to be integrated. This can be accompanied by numerical instabilities or excessive computation time and storage. The use of pencil glide systems can therefore become advantageous. The analyses of the previous sections show that the pencil glide model can mimic the results obtained considering  $\{110\} + \{112\}$  slip systems in many situations, even though significant differences have been evidenced in some loading cases.

Some comparisons between both approaches were performed in the past using the Taylor model for some limited loading conditions. In the present work the more general  $\beta$ -model was used and new situations were considered for comparison, namely the single crystal case, the simple shear of polycrystals and detailed analyses of tension, compression and rolling.

It must be emphasized that the final texture also depends on the interaction matrix and hardening parameters. On the one hand, 24 slip systems are used with the complete interaction matrix. On the other hand, the pencil glide approach makes use of a reduced interaction matrix. The full interaction matrix requires as much as 17 parameters: one for self-hardening, one for the dipolar interaction, twelve for junction formation and three for collinear annihilation. Some of them controls the activation of secondary slip system, that can be evidenced by the tension and compression tests. In the work [63], the authors used “full constraint” and “relaxed constraint” Taylor models. When glide is limited to  $\{112\}$  slip systems, the simulated texture is very sharp and the tube of orientations  $\{111\}(uuv)$  is not well described by any of these models. On the other hand, when glide is restricted to  $\{110\}$  systems, the simulations predict all the observed components. The simulated textures in this case are less sharp. A combination of the simulated textures however provides most of the features observed experimentally.

The collinear annihilations are known as the strongest interactions between dislocations because they decrease the length of dislocation sources [64]. It follows that collinear slip systems are not activated in many cases. This is in contrast to experimental observations showing that the cross slip mechanism is ubiquitous in b.c.c. crystals, so that dislocations can change plane to overcome obstacles. This is at the origin of the pencil glide mechanism. In the present work, we have still adopted the collinear annihilations as the strongest interaction in the matrix. Changing this value could result in significantly different final textures.

The  $\beta$ -model at large deformations used in the present work is an extended version of the one proposed in [21] where isotropic elasticity was assumed and the tensor  $\mathbb{D}$  was reduced to a scalar. Improvements are still needed like the account of grain shape changes during deformation. The presented  $\beta$ -model assumes that, in contrast to the strain rate tensor, the material spin is the same for all grains. Special localization rules should also be developed for the spin tensor.

## 6. Conclusion

The homogenization  $\beta$ -model at large deformations has been used to predict the crystallographic textures of b.c.c. metals when accounting for 24 slip systems or when introducing the pencil glide mechanism instead.

The effect was first analyzed in the case of single crystal behaviour including a detailed comparison with recent experimental results for  $\alpha$ -iron. For simple tension and compression of various single crystal orientations, no significant difference was found in the overall stress-strain curves and in lattice rotation whether pencil glide or the 24  $\{110\} + \{112\}$  slip systems were used.

In the rolling and simple shear tests where the number of slips systems and the interaction matrix control the texture, some discrepancies were found in the predictions based on pencil glide or  $\{110\} + \{112\}$  slip systems, especially at larger deformation values. These discrepancies are not significant for strain values below 100%.

Finally, it must be underlined that the computational time required for the pencil glide simulations is three times smaller than for the 24 slips systems. This lower computing time is a major advantage of the pencil glide approach. This makes the pencil glide model particularly well-suited for finite element simulations of alloy forming processes using polycrystal models which are still computationally demanding problems at the present time [28, 65].

## Dedication

Dedicated to Pierre Gilormini in remembrance of his early contributions on pencil glide modelling.

## Acknowledgements

This study was funded by Agence Nationale de la Recherche through the ANR TITWIP project (grant no. ANR-15-CE08-0013).

## Appendix A.

In this section, the parameterization of space rotations by means of exponential mapping used in the code is reviewed. Any rotation  $\mathbf{R}$  can be represented by the element  $\Phi$  of the associated Lie group such that:

$$\mathbf{R} = \exp(\mathbf{1} \times \Phi) \quad \text{and} \quad \Phi = \theta \mathbf{n} = [\Phi_1, \Phi_2, \Phi_3] \quad (22)$$

where  $\theta$  is the rotation angle (in radians) around a specified unit axis  $\mathbf{n}$ . One can rewrite the expression using the standard matrix exponential series, noting that:  $\exp(\mathbf{A}) = \sum_{k=0}^{\infty} 1/k! \mathbf{A}^k$ ,

$$\mathbf{R} = \exp(\mathbf{1} \times \Phi) = \cos \theta \mathbf{1} + \frac{1 - \cos \theta}{\theta^2} \Phi \otimes \Phi + \frac{\sin \theta}{\theta} \mathbf{1} \times \Phi. \quad (23)$$

In the matrix form:

$$\mathbf{R} = \begin{bmatrix} \cos \theta + \frac{1 - \cos \theta}{\theta^2} \Phi_1^2 & \frac{1 - \cos \theta}{\theta^2} \Phi_1 \Phi_2 - \frac{\sin \theta}{\theta} \Phi_3 & \frac{1 - \cos \theta}{\theta^2} \Phi_1 \Phi_3 + \frac{\sin \theta}{\theta} \Phi_2 \\ \frac{1 - \cos \theta}{\theta^2} \Phi_1 \Phi_2 + \frac{\sin \theta}{\theta} \Phi_3 & \cos \theta + \frac{1 - \cos \theta}{\theta^2} \Phi_2^2 & \frac{1 - \cos \theta}{\theta^2} \Phi_2 \Phi_3 - \frac{\sin \theta}{\theta} \Phi_1 \\ \frac{1 - \cos \theta}{\theta^2} \Phi_1 \Phi_3 - \frac{\sin \theta}{\theta} \Phi_2 & \frac{1 - \cos \theta}{\theta^2} \Phi_2 \Phi_3 + \frac{\sin \theta}{\theta} \Phi_1 & \cos \theta + \frac{1 - \cos \theta}{\theta^2} \Phi_3^2 \end{bmatrix} \quad (24)$$

Defining the spin tensor  $\mathbf{R}\mathbf{R}^T = \mathbf{L}$ , the following relation can be worked out:

$$\mathbf{\dot{\Phi}} = \mathbf{T}^{-1} \mathbf{\dot{\Omega}} \tag{25}$$

Note that any skew-symmetric matrix  $\mathbf{\Omega}$  can be represented by the pseudo-vector  $\mathbf{\dot{\Omega}}$  such that:  $\mathbf{\Omega}\mathbf{b} = \mathbf{\dot{\Omega}} \times \mathbf{b}$ . In matrix form:

$$\mathbf{\Omega} = \begin{bmatrix} 0 & -\mathbf{\dot{\Omega}}_3 & \mathbf{\dot{\Omega}}_2 \\ \mathbf{\dot{\Omega}}_3 & 0 & -\mathbf{\dot{\Omega}}_1 \\ -\mathbf{\dot{\Omega}}_2 & \mathbf{\dot{\Omega}}_1 & 0 \end{bmatrix} \quad \text{so that } \mathbf{\dot{\Omega}} = [\mathbf{\dot{\Omega}}_1, \mathbf{\dot{\Omega}}_2, \mathbf{\dot{\Omega}}_3]^T \tag{26}$$

The matrix form of the operator  $\mathbf{T}$  is

$$\mathbf{T} = \begin{bmatrix} \frac{\sin\theta}{\theta} + \frac{1 - \frac{\sin\theta}{\theta}}{\theta^2} \Phi_1^2 & \frac{1 - \frac{\sin\theta}{\theta}}{\theta^2} \Phi_1 \Phi_2 - \frac{1 - \cos\theta}{\theta^2} \Phi_3 & \frac{1 - \frac{\sin\theta}{\theta}}{\theta^2} \Phi_1 \Phi_3 + \frac{1 - \cos\theta}{\theta^2} \Phi_2 \\ \frac{1 - \frac{\sin\theta}{\theta}}{\theta^2} \Phi_1 \Phi_2 + \frac{1 - \cos\theta}{\theta^2} \Phi_3 & \frac{\sin\theta}{\theta} + \frac{1 - \frac{\sin\theta}{\theta}}{\theta^2} \Phi_2^2 & \frac{1 - \frac{\sin\theta}{\theta}}{\theta^2} \Phi_2 \Phi_3 - \frac{1 - \cos\theta}{\theta^2} \Phi_1 \\ \frac{1 - \frac{\sin\theta}{\theta}}{\theta^2} \Phi_1 \Phi_3 - \frac{1 - \cos\theta}{\theta^2} \Phi_2 & \frac{1 - \frac{\sin\theta}{\theta}}{\theta^2} \Phi_2 \Phi_3 + \frac{1 - \cos\theta}{\theta^2} \Phi_1 & \frac{\sin\theta}{\theta} + \frac{1 - \frac{\sin\theta}{\theta}}{\theta^2} \Phi_3^2 \end{bmatrix} \tag{27}$$

The rotation angle can be obtained from the rotation matrix  $\mathbf{R}$  by the following operation:

$$\theta = \arccos\left(\frac{\text{trace}(\mathbf{R}) - 1}{2}\right) \tag{28}$$

and, if  $\theta \neq 0$  and  $\mathbf{R}_{ij}$  are the components of  $\mathbf{R}$ , the rotation axis is

$$\mathbf{n} = \frac{\mathbf{\Phi}}{\theta} = \frac{1}{2\sin\theta} [R_{32} - R_{23}, R_{13} - R_{31}, R_{21} - R_{12}] \tag{29}$$

### Appendix B.

Each grain is represented by an ellipsoidal inclusion  $(a_1, a_2, a_3)$  embedded in a homogeneous effective medium (HEM) resulting from the average over all the grains. The Eshelby tensor  $\mathbb{S}^{\text{Esh}}$  is calculated by using the Green function that depends on the inclusion shape and the elasticity tensor of the HEM  $\mathbb{C}^{\text{Homo}}$ :

$$\mathbb{S}_{ijkl}^{\text{Esh}} = \frac{\mathbb{C}_{mnlk}^{\text{Homo}}}{8\pi} \int_{-1}^1 d\zeta_3 \int_0^{2\pi} [\mathbb{G}_{imjn}(\xi) + \mathbb{G}_{jmin}(\xi)] d\omega \tag{30}$$

with

$$\mathbb{G}_{ijkl}(\xi) = \xi_k \xi_l \frac{N_{ij}(\xi)}{D(\xi)} \tag{31}$$

$$\xi_1 = \frac{\sqrt{1 - \zeta_3^2}}{a_1} \cos\omega, \quad \xi_2 = \frac{\sqrt{1 - \zeta_3^2}}{a_2} \sin\omega, \quad \xi_3 = \frac{\zeta_3}{a_3} \tag{32}$$

$$K_{ik} = \mathbb{C}_{ijkl}^{\text{Homo}} \xi_j \xi_l \tag{33}$$

$$N_{ij}(\xi) = \frac{1}{2} \epsilon_{ijk} \epsilon_{jmn} K_{km} K_{ln} \tag{34}$$

$$D(\xi) = \epsilon_{mnl} K_{m1} K_{n2} K_{l3} \tag{35}$$

$\epsilon_{ijk}$  is the Levi-Civita symbol. The Gaussian quadrature method is used to compute the integration in (22):

$$\mathbb{S}_{ijkl}^E = \frac{\mathbb{C}_{mnlk}^{\text{Homo}}}{8\pi} \sum_{p=1}^M \sum_{q=1}^N [\mathbb{G}_{imjn}(\omega_q, \zeta_{3p}) + \mathbb{G}_{jmin}(\omega_q, \zeta_{3p})] W_{pq} \tag{36}$$

Here  $M$ ,  $N$  are the number of nodes, and  $W_{pq}$  are the weights at the Gauss points. In the present article, the values  $M = 32$  and  $N = 32$  are applied.

## References

- [1] P. Gilormini, "The theory of rate sensitive pencil glide application to rolling textures", *Acta Metall.* **37** (1989), p. 2093-2101.
- [2] L. Le, P. Franciosi, "Expectable specific features of BCC crystal plastic flow and consistency with the Schmid law", *Phil. Mag.* **93** (2013), p. 3589-3611.
- [3] P. Franciosi, L. Le, G. Monnet, C. Kahloun, M.-H. Chavanne, "Investigation of slip system activity in iron at room temperature by SEM and AFM in-situ tensile and compression tests of iron single crystals", *Int. J. Plast.* **65** (2015), p. 226-249.
- [4] G. Taylor, C. Elam, "The distortion of iron crystals", *Proc. R. Soc. Lond. A* **112** (1926), p. 337-361.
- [5] P. Gilormini, B. Bacroix, J. Jonas, "Theoretical analyses of  $\langle 111 \rangle$  pencil glide in b.c.c. crystals", *Acta Metall.* **36** (1988), p. 231-256.
- [6] R. Becker, "Pencil glide formulation for polycrystal modelling", *Scr. Metall. Mater.* **32** (1995), p. 2051-2054.
- [7] G. Taylor, "Plastic strain in metals", *J. Inst. Metals* **62** (1938), p. 307-324.
- [8] G. Sachs, "Zur Ableitung einer Fließbedingung", *Z. Verein. Dtsch. Ing.* **72** (1928), p. 734-736.
- [9] J. Bishop, R. Hill, "A theory of the plastic distortion of a polycrystalline aggregate under combined stresses", *Lond. Edinburgh Dublin Phil. Mag. J. Sci.* **42** (1951), no. 327, p. 414-427.
- [10] H. Honnef, H. Mecking, "A method for the determination of the active slip systems and orientation changes during single crystal deformation", in *Proceedings of the 5th International Conference on Texture of Materials*, Springer Verlag, 1978, p. 265-275.
- [11] H. Mecking, "Low temperature deformation of polycrystals", in *Proceedings of the 2th International Symposium on Metallurgy and Materials Science: Deformation of Polycrystals*, Danmarks Tekniske Universitet, 1981, p. 73-86.
- [12] U. Kocks, G. Canova, "How many slip systems and which?", in *Deformation of polycrystals: Mechanisms and Microstructures, 2nd International Symposium on Metallurgy and Materials Science* (N. Hansen, A. Horsewell, T. Leffers, H. E. Liholt, eds.), Risø National Laboratory, Roskilde, Denmark, 1981, p. 35-44.
- [13] P. Van Houtte, "On the equivalence of the relaxed Taylor theory and the Bishop-Hill theory for partially constrained plastic deformation of crystals", *Mater. Sci. Eng.* **55** (1982), p. 69-77.
- [14] M. Arminjon, "Théorie d'une classe de modèles de Taylor Hétérogènes: application aux textures de déformation des aciers", *Acta Metall.* **35** (1987), p. 615.
- [15] M. Arminjon, C. Donadille, "Présentation d'un modèle polycristallin extrême: application aux aciers d'un modèle approché", *Mém. Et. Sci. Revue Métall.* **87** (1990), p. 359.
- [16] A. Molinari, "Extensions of the self-consistent tangent model", *Model. Simul. Mater. Sci. Eng.* **7** (1999), p. 683-697.
- [17] R. Lebensohn, C. Tome, "A self-consistent visco-plastic model: calculation of rolling textures of anisotropic materials", *Mater. Sci. Eng. A* **175** (1994), p. 71-82.
- [18] M. Berveiller, A. Zaoui, "An Extension of the self-consistent scheme to plastically flowing polycrystals", *J. Mech. Phys. Solids* **26** (1979), p. 325-344.
- [19] P. Lipinski, J. Krier, M. Berveiller, "Elastoplasticité des métaux en grandes déformations: comportement global et évolution de la structure interne", *Rev. Phys. Appl.* **25** (1990), p. 361-388.
- [20] G. Cailletaud, "A micromechanical approach to inelastic behaviour of metals", *Int. J. Plast.* **8** (1992), p. 55-73.
- [21] S. Forest, P. Pilvin, "Modelling finite deformation of polycrystals using local objective frames", *Z. Angew. Math. Mech.* **79** (1999), p. 199-202.
- [22] K. Sai, G. Cailletaud, S. Forest, "Micro-mechanical modeling of the inelastic behavior of directionally solidified materials", *Mech. Mat.* **38** (2006), no. 3, p. 203-217.
- [23] G. Martin, N. Ochoa, K. Sai, E. Hervé-Luanco, G. Cailletaud, "A multiscale model for the elastoviscoplastic behavior of directionally solidified alloys: application to FE structural computations", *Int. J. Solids Struct.* **51** (2014), p. 1175-1187.
- [24] G. Cailletaud, F. Coudon, "Scale transition rules applied to crystal plasticity", in *Materials with Internal Structure: Multiscale and Multifield Modeling and Simulation* (P. Trovalusci, ed.), Springer International Publishing, 2016, p. 1-15.
- [25] F. Coudon, G. Cailletaud, J. Cormier, L. Marciniak, "A multiscale model for nickel-based directionally solidified materials", *Int. J. Plast.* **115** (2019), p. 1-17.
- [26] P. Pilvin, "Une approche inverse pour l'identification d'un modèle polycristallin élastoviscoplastique", in *3ème Colloque National en Calcul des Structures, 20-23 mai, Giens*, Presses Académiques de l'Ouest, 1997, p. 207-212.
- [27] J. Besson, G. Cailletaud, J.-L. Chaboche, S. Forest, M. Blétry, in *Non-Linear Mechanics of Materials, Solid Mechanics and Its Applications*, vol. 167, Springer-Verlag, Berlin, Heidelberg, 2009.

- [28] N. Hfaiedh, A. Roos, H. Badreddine, K. Saanouni, "Interaction between ductile damage and texture evolution in finite polycrystalline elastoplasticity", *Int. J. Damage Mech.* **28** (2019), p. 481-501.
- [29] J. Mandel, "Equations constitutives et directeurs dans les milieux plastiques et viscoplastiques", *Int. J. Solids Struct.* **9** (1973), p. 725-740.
- [30] A. Krawietz, "Efficient integration in the plasticity of crystals with pencil glide and deck glide", *Tech. Mech.* **21** (2001), p. 243-250.
- [31] R. Glüge, "Glide mechanisms for bundle- and plate-like structures", *Tech. Mech.* **35** (2015), p. 62-69.
- [32] C. Guillemer, M. Clavel, G. Cailletaud, "Cyclic behavior of extruded magnesium: experimental, microstructural and numerical approach", *Int. J. Plast.* **27** (2011), p. 2068-2084.
- [33] M. Lindroos, G. Cailletaud, A. Laukkanen, V.-T. Kuokkala, "Crystal plasticity modeling and characterization of the deformation twinning and strain hardening in Hadfield steels", *Mat. Sci. Eng.* **720** (2018), p. 145-159.
- [34] P. Pilvin, "The Contribution of Micromechanical Approaches to the Modelling of Inelastic Behaviour of Polycrystals", in *Fourth Int. Conf. on Biaxial/multiaxial Fatigue and Design (London)* (A. Pineau, G. Cailletaud, T. Lindley, eds.), ESIS, vol. 21, Mechanical Engineering Publications, 1996, p. 3-19.
- [35] G. Martin, L. Nazé, G. Cailletaud, "Numerical multi-scale simulations of the mechanical behavior of  $\beta$ -metastable titanium alloys Ti5553 and Ti17", *Procedia Eng.* **10** (2011), p. 1803-808.
- [36] P. Pilvin, F. Onimus, R. Brenner, S. Pascal, X. Feaugas, K. Săi, "Finite element assessment of an affine self-consistent model for hexagonal polycrystals", *Eur. J. Mech. - A/Solids* **61** (2017), p. 345-356.
- [37] T. Gu, J.-R. Medy, V. Klosek, O. Castelnaud, S. Forest, E. Hervé-Luanco, F. Lecouturier-Dupouy, H. Proudhon, P.-O. Renault, L. Thilly, P. Villechaise, "Multiscale modeling of the elasto-plastic behavior of architected and nanostructured Cu-Nb composite wires and comparison with neutron diffraction experiments", *Int. J. Plast.* **122** (2019), p. 1-30.
- [38] A. Bertram, M. Kraska, "Determination of finite plastic deformations in single crystals", *Arch. Mech.* **47** (1995), p. 203-222.
- [39] D. Caillard, "Kinetics of dislocations in pure Fe. Part I. In situ straining experiments at room temperature", *Acta Mater.* **58** (2010), p. 3493-3503.
- [40] J. Kumagai, S. Takaki, S. Suzuki, H. Kimura, "Orientation dependence of quasi-three-stage work hardening in high purity iron single crystals", *Mater. Sci. Eng. A* **129** (1990), no. 2, p. 207-215.
- [41] B. Jaoul, *Etude de la plasticité et application aux métaux, 1st published*, Presses des Mines de Paris, 1965.
- [42] G. Monnet, D. Terentyev, "Structure and mobility of the edge dislocation in BCC iron studied by molecular dynamics", *Acta Mater.* **57** (2009), no. 5, p. 1416-1426.
- [43] S. Queyreau, J. Marian, M. Gilbert, B. Wirth, "Edge dislocation mobilities in bcc Fe obtained by molecular dynamics", *Phys. Rev. B* **84** (2011), no. 6, article no. 064106.
- [44] C. Domain, G. Monnet, "Simulation of screw dislocation motion in iron by molecular dynamics simulations", *Phys. Rev. Lett.* **95** (2005), no. 21, article no. 215506.
- [45] P. Franciosi, "Etude théorique et expérimentale du comportement élastoplastique des monocristaux métalliques se déformant par glissement : modélisation pour un chargement complexe quasi-statique", PhD Thesis, Université Paris 13, 1984.
- [46] R. Madec, L. Kubin, *Dislocation Interactions and Symmetries in BCC Crystals*, Springer, Netherlands, 2004, 69-78 pages.
- [47] R. Madec, B. Devincere, L. Kubin, "From dislocation junctions to forest hardening", *Phys. Rev. Lett.* **89** (2003), article no. 255508.
- [48] L. P. Kubin, R. Madec, B. Devincere, "Dislocation intersections and reactions in FCC and BCC crystals", *MRS Proc.* **779** (2003), article no. W1.6.
- [49] R. Madec, B. Devincere, L. Kubin, T. Hoc, D. Rodney, "The role of collinear interaction in dislocation-induced hardening", *Science* **301** (2003), p. 1879-1882.
- [50] S. Queyreau, G. Monnet, B. Devincere, "Slip systems interactions in  $\alpha$ -iron determined by dislocation dynamics simulations", *Int. J. Plast.* **25** (2009), no. 2, p. 361-377.
- [51] L. T. Le, "Etude par essais in situ MEB et AFM sur monocristaux des mécanismes de glissement à température ambiante de la ferrite de pureté commerciale", PhD Thesis, Université Paris Nord, 2013.
- [52] E. Bruder, "Mechanical properties of ARMCO<sup>®</sup> iron after large and severe plastic deformation-application potential for precursors to ultrafine grained microstructures", *Metals* **8** (2018), p. 191-203.
- [53] P. Coulomb, *Les textures dans les métaux de réseau cubique*, Dunod, Paris, France, 1972.
- [54] U. Kocks, C. Tomé, H. R. Wenk, *Texture and Anisotropy*, Cambridge University Press, 1998.
- [55] A. Das, "Calculation of crystallographic texture of BCC steels during cold rolling", *J. Mat. Eng. Perform.* **26** (2017), no. 6, p. 2708-2720.
- [56] D. Ceccaldi, F. Yala, T. Baudin, R. Penelle, F. Royer, M. Arminjon, "Deformation textures and plastic anisotropy of steels using the Taylor and nonhomogeneous models", *Int. J. Plast.* **10** (1994), p. 643-661.

- [57] M. Hoelscher, D. Raabe, K. Luecke, "Rolling and recrystallization textures of BCC steels", *Steel Res. Int.* **62** (1991), p. 567-575.
- [58] S. M'Guil, W. Wen, S. Ahzi, J. J. Gracio, "Modeling of large plastic deformation behavior and anisotropy evolution in cold rolled bcc steels using the viscoplastic  $\phi$ -model-based grain-interaction", *Mat. Sci. Eng.: A* **528** (2011), p. 5840-5853.
- [59] D. Raabe, "Investigation of contribution of {123} slip planes to development of rolling textures in bcc metals by use of Taylor models", *Mater. Sci. Technol.* **11** (1995), p. 455-460.
- [60] J. Baczynski, J. J. Jonas, "Texture development during the torsion testing of  $\alpha$ -iron and two IF steels", *Acta Mater.* **44** (1996), p. 4273-4288.
- [61] O. W. Williams, "Shear texture in copper, brass, aluminum, iron and zirconium", *Trans. Metall. Soc. AIME* **224** (1962), p. 129-139.
- [62] C. Kahloun, G. Monnet, S. Queyreau, L. Le, P. Franciosi, "A comparison of collective dislocation motion from single slip quantitative topographic analysis during in-situ AFM room temperature tensile tests on Cu and Fe $\alpha$  crystals", *Int. J. Plast.* **84** (2016), p. 277-298.
- [63] J. L. Raphanel, P. Van Houtte, "Simulation of the rolling textures of b.c.c. metals by means of the relaxed taylor theory", *Acta Metall.* **33** (1985), p. 1481-1488.
- [64] L. P. Kubin, R. Madec, B. Devincere, "Dislocation intersections and reactions in FCC and BCC crystals", *MRS Proc.* **779** (2003), article no. W1.6.
- [65] G. Cailletaud, P. Pilvin, "Utilisation de modèles polycristallins pour le calcul par éléments finis", *Rev. Européenne des Éléments Finis* **3** (1994), p. 515-541.